Compositional Effects on the Mechanical Properties and Deformation Mechanisms of Face-Centered Cubic High-Entropy Alloys

A Dissertation Presented for the
Doctor of Philosophy
Degree
The University of Tennessee, Knoxville

Joshua Lee Cicotte
December 2022

Acknowledgments

I would like to extend my deep gratitude to my advisor, Easo George. Thank you for giving me the freedom to explore and for acting as my guiderail when I strayed too far. I appreciate the kindness and patience you have shown me and your willingness to make time for me. I would like to thank Ying Yang and Weicheng Zhong for your support and mentorship. I appreciate the time we have spent together, and I will miss our weekly meetings! Thank you for your guidance.

I would also like to thank Veerle Keppens, Brianna Musico, and Candice Kinsler-Fedon for their assistance with the RUS measurements that have provided clarity to my work. I would like to thank Michael Koehler and Claudia Rawn for their expertise and help with X-ray diffraction.

And I would like to thank Jeff Brookins, Jack Carpenter, and Ian Stinson. You guys helped me keep my sanity through the many hurtles of working at the lab and all the red tape we encountered. Thank you, Ian, for continually putting up with our shenanigans and teaching us the basics of machining. Without your support, none of this could have been accomplished.

To my family, thank you for always being only a phone call away. Your support and encouragement have been indispensable, and I would not have achieved my dreams without you.

I was supported by the Basic Energy Sciences program through the U.S. Department of Energy and by the University of Tennessee's Governor's Chair program.

Abstract

High entropy alloys, HEAs, have expanded the compositional spaces of modern metallurgy into highly concentrated and chemically complex alloys, previously believed to be unproductive. With this newfound compositional freedom, comes additional control, allowing for new investigations into previously established mechanisms. To discover new and potentially useful alloys, the HEA field is continually expanding away from the equiatomic solid solutions that dominated early work. The work presented in this dissertation utilizes two, intuitive, pseudo-binary HEA systems to investigate compositional effects on solid solution strengthening in highly concentrated alloys and twinning and transformation induced plasticity. It furthers the understanding of the mechanical properties of concentrated alloys and their deformation mechanisms.

Table Of Contents

List Of Tables

List Of Figures

Introduction

Traditionally, most metal alloys have consisted of a single primary metal with small additions of other elements. The designs of these alloys focused on the properties of the principal metal with alloying additions chosen to enhance certain properties, such as adding Ni to steels to increase the hardenability [1], or address weaknesses, like adding small amounts of Mn to steels to precipitate S as sulfides to increase hot formability [2]. Some traditionally designed alloys do utilize more complex compositions, such as Ni superalloys or many stainless steels. However, the design of these alloys follows the above path with focus placed on a principal or base metal: Ni superalloys are still Ni based-alloys, and stainless steels are still ferrous alloys. Cantor et al. [3] and Yeh et al. [4] were some of the first to break out of this mold.

Cantor et al. found a relatively unusual alloy that consisted of Cr, Mn, Fe, Co, and Ni in equal parts, which formed a face-centered cubic (FCC) solid solution [3]. Both the crystal structure and solid solution state were quite surprising. Alloying elements with different crystal structures often limits their mutual solubility, yet of the five elements, only Ni is FCC at room temperature [5, 6]. Similarly, increasing the number of elements, especially in high concentrations, typically increases the chances of intermetallics forming. Yeh et al. [4] proposed that it was the large number of elements in equal proportions that offered increased solubility by increasing the configurational entropy of the system, i.e., the high-entropy effect. With this proposed stabilizing effect, Yeh et al. [4] also hypothesized that the physical properties of HEAs could be unique. This sparked the initial interest and focus on equiatomic solid solution HEAs. However, Otto et al. [7] demonstrated that high configurational entropy was not responsible for stabilizing solid solutions in equiatomic alloys, and Wu et al. [8] demonstrated that there was no correlation between the magnitude of configurational entropy and the mechanical properties of equiatomic solid solution alloys. Subsequently, Li et al. [9] demonstrated that by moving to off-equiatomic compositions the strength and ductility of HEAs can be enhanced. In other words, alloy composition (and the nature of the constituent elements) determined microstructure and properties, not the number of elements added or their strict equiatomic proportions.

Interest therefore spread to the vast compositional space away from the initial equiatomic solid solution HEAs. These alloys are sometimes referred to as complex concentrated alloys (CCAs), multiprincipal component alloys (MPCAs) or medium entropy alloys (MEAs) but for simplicity, the term HEA will be used here. The freedom of the large compositional spaces and many alloying additions found in non-equiatomic HEAs allows for greater experimental control when investigating the mechanisms dictating the physical properties of alloys. For example, experiments in the Fe-Mn system examining the role of composition on deformation mechanisms inevitably vary the shear modulus, magnetic state, driving forces of martensitic transformations, and stacking fault energy (SFE) simultaneously as there are too few compositional variables to control all these factors independently [10-12]. In a recent Cr-Mn-Fe-Co-Ni HEA system, a compositional range was identified over which *only* the SFE is varied, opening the possibility of highly controlled experiments with fewer confounding factors [13]. This process, however, is very intensive and requires considerable experimental effort. Pseudo-binary HEAs offer a middle-ground approach with systematic changes in composition that offer the wide ranges in composition available in HEAs but with enough control to understand any confounding changes in physical properties without requiring a significant characterization effort. These alloy designs usually focus on varying two elements or groups of elements at a time to investigate the microstructure, mechanical properties, and deformation mechanisms [9, 13-21].

This dissertation focuses on the compositional dependence of several strengthening and deformation mechanisms utilizing intuitive pseudo-binary HEAs. Chapter I investigates the role of composition and atomic displacements from ideal lattice sites on the degree of solid solution strengthening through the Co_{25}-Mn_{25}-Ni_{25}-$Fe_{(x)}$-$Cr_{(25-x)}$ system (all compositions in this dissertation, are in at%, unless otherwise noted). Chapters II and III utilize a Cr_{33}-$Co_{(x)}$-$Ni_{(67-x)}$ system to investigate compositional effects on twinning induced plasticity (TWIP) and transformation induced plasticity (TRIP) respectively.

Chapter I
Compositional Dependence of Solid Solution Strengthening in a Pseudo-Binary High Entropy Alloy

A version of this chapter is being prepared for publication in a peer reviewed journal. Joshua Cicotte performed all experimental work and writing. Jefferey Brookins and Candice Kinsler-Fedon assisted with the collection and analysis of RUS data. Easo George conceived the study and supervised the project.

Introduction

Solid solution alloys are formed by the addition of solute atoms to a solvent. The solubility of one metal in another is governed by several physical and chemical properties including differences in crystal structure, atomic size, and electronegativity [5]. Metals with the same crystal structure and similar atomic sizes are generally mutually soluble although solutes are generally more soluble if the solvent has a lower valence [5, 22]. The differences in atomic size and shear modulus between the solvent and solute produces a strain field around solutes which interacts with the strain field around dislocations to impede their motion, providing a strengthening effect proportional to the concentration of the solute [22]. Several iterations of models have been developed to relate the concentration and properties of the solute and solvent to solid solution strengthening. As will be discussed below, the early models were developed for dilute solid solutions (typically binaries) and encounter difficulties when applied to concentrated solid solutions. Similarly, equiatomic alloys pose conceptual problems for most models because they lack "solvents" and "solutes" in the traditional sense (each element in an equiatomic alloy may be viewed as a solvent or solute).

The first solid solution model, proposed by Mott and Nabarro, uses the difference in size between solvent and solute atoms (often referred to as atomic misfit) to estimate a lattice distortion or strain [23, 24]. While this strain can be directly measured through diffraction techniques, it was incapable of fully capturing solid solution strengthening effects. Particularly, the model cannot be applied when plastic deformation is dominated by screw dislocations, as these dislocations do not interact with the purely dilatational strains generated by atomic misfit [24]. Fleischer added to the atomic misfit model by including a shear modulus misfit [24]. The modulus misfit effect arises from the local variation in elastic stiffness near a solute atom and contributes to solute interactions with gliding dislocations that result in a compositional dependence of the form $C_{solute}^{1/2}$[24]. The shear modulus mismatch can also explain the interactions between screw dislocations and solutes that cannot be explained by atomic mismatch alone. However, the model is restricted to the interaction between dislocations and a single solute atom on an adjacent glide plane. This limits the applicable solute-dislocation interaction forces and restricts the composition to very dilute systems [24]. Labusch introduced a statistical approach to the distribution of solute atoms and their interactions with dislocations [25, 26]. This creates a range of solute-dislocation interactions that more accurately represents solid solutions with solute concentrations up to several atomic percent resulting in a $C_{solute}^{2/3}$ dependency. Additionally, Labusch's model allows for dislocations to bend around solute obstacles and identifies the relative contributions of atomic and modulus mismatch to the strengthening effect [25, 26]. Leyson et. al recently expanded upon Labusch's model through first principles calculations of the solute-dislocation interaction energies [27-29]. This allowed for the calculation of the critical resolved shear stress in several Al and Mg alloys and included both temperature and compositional dependencies [27-29].

The above models all describe relatively dilute solid solutions in which there are clear solutes and solvents. HEAs, however, are complex, concentrated solid solutions of many elements, often in equiatomic or near equiatomic proportions. This offers a fundamental challenge to the basis of traditional solid solution models as there are no solvents or solutes. Currently, there are

three proposed methods to model HEAs, two of which extend traditional models to concentrated solutions, and a third that utilizes atomic displacement as a scaling factor.

To apply Labusch's dilute model to HEAs, Toda-Caraballo et al. [30] rely on calculating an average lattice parameter and shear modulus using Vegard's law. From this, an average atomic misfit and modulus misfit can be used in Labusch's model to estimate the solid solution strengthening effect. Likewise, Varvenne et al. [31, 32] adapted Leyson's et al. dilute solid solution model to HEAs by creating an "effective medium" from the average properties of the alloy (i.e., the shear modulus, atomic volumes, lattice parameter, and Burger's vector). Each alloying addition is added to the effective medium as an isolated solute atom, allowing for the application of Layson's model. Both adaptions rely heavily on accurate atomic radii as these are needed for calculating the atomic volumes and misfits used to estimate the degree of solid solution strengthening [30-32]. This is a challenge in simple alloys let alone HEAs where several alloying elements are not in their room temperature crystal structures and are dissolved in highly concentrated solutions [31-34].

A third, more direct route was proposed by Okamoto et al. [33], in which the displacement of atoms from their ideal lattice positions can be measured and correlated to the yield strength of concentrated solid solutions. At 0K, all atoms in an HEA experience this displacement as each atom is surrounded by a unique atomic neighborhood and need to accommodate the different atomic sizes. At higher temperatures, additional displacements about the mean position occur due to thermal vibrations. Okamoto et al. [33] used single-crystal synchrotron X-ray diffraction to measure the mean square atomic displacement (MSAD) which captured the average displacement of all atoms in the equiatomic CrMnFeCoNi alloy. To understand how each individual element might affect the atomic displacement, first-principles calculations were utilized as the individual atomic displacement parameters (ADPs) could not be determined using diffraction [33]. From the elemental ADPs, an average MSAD for the equiatomic CrMnFeCoNi alloy was then calculated and it was found to be comparable to the MSAD determined from the diffraction experiments. Furthermore, it was shown that the square-root-(MSAD) scales with the yield stress of several equiatomic alloys within the Cr-Mn-Fe-Co-Ni family and that Cr produces the largest displacement of atoms [33]. Importantly, Okamoto et al. [33] found that the strength and MSAD were dependent on the specific elements present in an alloy and did not correlate with the number of elements present in the alloy, an early hypothesis of HEAs [4, 33].

To further understand the relationship between composition, atomic displacement, and solid solution strengthening, a pseudo-binary system of alloys was investigated in the present study using the alloys explored in Okamoto et al. [33] as a guide. The two most extreme alloys previously investigated are CoCrNiMn, which possesses the largest MSAD and yield strength, and CoFeNiMn which possesses the smallest MSAD and yield strength [33]. Using these alloys as the end points of the pseudo-binary system, we kept the Co, Ni, and Mn contents constant at 25% each while the remaining 25% was systematically varied from Cr to Fe. This forms a relatively simple system of alloys, Co_{25}-Ni_{25}-Mn_{25}-$Fe_{(x)}$-$Cr_{(25-x)}$ which can be systematically investigated for changes in MSAD and strength to investigate, and any possible correlations between the two.

Methods

Processing

A pseudo-binary system of alloys with the compositions Co_{25}-Ni_{25}-Mn_{25}-$Fe_{(x)}$-$Cr_{(25-x)}$ where x = 0, 5, 10, 15, 20, and 25% was fabricated by arc melting the constituent elements (purity

>99.99%) into buttons in an Ar atmosphere in a water-cooled copper crucible. The buttons were flipped and remelted five times to ensure the alloys were thoroughly mixed before drop-casting into a 12.7mm x 25.4mm x 127mm rectangular mold. The ingots were encapsulated in evacuated quartz tubes backfilled with Ar and homogenized at 1200°C for 48h followed by a quench into room temperature water. The quartz tubes shattered on contact with the water and the samples were stirred to assure a rapid quench. The ingots were cold rolled to a thickness of 4.75mm (~60% reduction) and annealed at 1000°C for 15 minutes followed by a quench into room temperature water to produce a fully recrystallized, equiaxed grain structure and to suppress secondary phase formation.

Characterization

X-ray diffraction (XRD) with Cu Kα radiation was used to characterize the microstructure and measure the lattice parameter of each alloy. Additionally, backscatter electron (BSE) micrographs were captured to ensure no additional phases were present below the detection limit of XRD. Grain size and texture were characterized using electron backscattering diffraction (EBSD). The grain size was measured by the linear intercept method. The composition of each alloy was measured using energy dispersive x-ray spectroscopy (EDS) at 15 KeV with a live detector time of 10 minutes.

Resonant ultrasound spectroscopy (RUS) was utilized to measure the elastic constants of each alloy to account for the compositional dependence of the shear modulus. To ensure a high degree of perpendicularity, RUS samples were prepared by surface grinding a portion of the recrystallized bar to a thickness of 4 mm and cut nominally into 4 mm x 5 mm x 6 mm cuboids using a diamond blade. Samples were excited at discrete intervals of 10 Hz between 300 kHz and 1.5 MHz. Each sample was mounted both corner to corner and edge to edge to ensure all resonances were detected over this range. Between 60 and 80 resonances were measured and used to calculate the elastic constants. The root-mean-square error of each fit was less than 0.5%.

Tensile Testing

The mechanical properties of each alloy were measured using tensile testing with a contact extensometer to measure strain. Tensile bars were cut from the recrystallized material using wire electrical discharge machining (EDM) with a 10 mm x 2 mm x 1 mm gauge section and were polished to a 600-grit finish. A constant crosshead displacement rate of 10^{-2} mm s^{-1} provided an engineering strain rate of 10^{-3} s^{-1}. The yield stress was determined using the 0.2% strain offset method. Three tests were performed for each alloy.

Results and Discussion

Microstructure

The microstructure of each alloy comprises a single solid solution FCC phase with equiaxed grains, as shown in the BSE micrographs in Figure I-1. No phase contrast is visible, with the exception of a small volume fraction of spherical oxide inclusions introduced during casting (appearing as black particles.) These oxide particles do not significantly impact the mechanical properties of the alloys due to their relatively large size and low volume fraction. EBSD was utilized to characterize the size and texture of the grain structure after cold rolling and annealing. Inverse pole figure grain maps shown in Figure I-2 and the inverse pole figures in Figure I-3 show little residual texture from thermomechanical processing with slight variations of approximately

1.5 to 2 times above random texture. Table I-1 shows the 'grain' size with and without the annealing twins included in the intercept count (the former is referred to as the 'crystallite' size); both increase gradually with Fe content. The average composition of each alloy measured by EDS is found in Table I-2.

The x-ray diffraction patterns in Figure I-4 contain solely FCC reflections (the oxide particles visible in Figure I-1 are below the detection limit.) Figure I-5 shows the lattice parameter of each alloy calculated from the diffraction patterns using the Nelson-Riley function [35, 36]. The lattice parameter increases with Cr content, reaching a maximum in the 0% Fe alloy, CrMnCoNi. This agrees well with the results of Okamoto et al. where it was shown that Cr produces the largest atomic displacements in the Cr-Mn-Fe-Co-Ni family of alloys [33]. In our pseudo-binary system, as Fe is replaced with Cr, the average displacement of atoms increases, forcing the unit cell to expand. This is similar to many binary solid solutions, in which the lattice parameter scales with the atomic size and concentration of solute added to the system [37]. Because of their physical connection, the lattice parameter will be used as a substitute for the mean-square atomic displacement when considering the relationship between composition and solid solution strengthening.

Mechanical Properties

Tensile testing revealed a strong linear correlation between the composition (Cr/Fe content) and both the yield strength and ultimate tensile strength, as shown in Figure I-6. Both yield and tensile strengths increase with Cr content, with a maximum of 282 MPa and 646 MPa respectively in CoMnNiCr (x = 0) and a minimum of 184 MPa and 520 MPa respectively in CoMnNiFe (x = 25). These end-point values in the pseudo-binary system agree well with previous results for equiatomic alloys [8]. A full summary of the tensile properties is found in Table I-3. Figure I-7 shows representative stress-strain curves and work hardening rates for each alloy. Despite the steady increase in strength with Cr concentration, the uniform elongation remains roughly constant at approximately 40%. A slight increase in the work hardening rate with the Cr content is responsible for delaying plastic instability with the increase in strength.

Factors that affect strength include solid solution strengthening, Hall-Petch strengthening, precipitate strengthening, and texture strengthening. Since the alloys all had nearly random texture and were largely free of secondary phases, only Hall-Petch strengthening and solid solution strengthening can be responsible for the differences in the yield strength of the different alloys discussed above. The Hall-Petch relationship, eq(1), describes the strengthening provided by grain boundaries in polycrystalline metals and consists of two parts: an intrinsic 'lattice friction', σ_o, which is the resistance of the matrix to the motion of dislocations and a 'locking parameter', k, which describes the resistance of dislocation transmission across grain boundaries and scales with the grain size, d [38-40].

$$\sigma = \sigma_o + kd^{-1/2} \quad \text{eq(1)}$$

The lattice friction term, σ_o, contains contributions from solid solution strengthening and therefore should not be subtracted from the yield strength, only the grain size dependent term ($kd^{-1/2}$) should be removed [40]. These constants have been reported for the equiatomic alloy CoFeMnNi (Fe25) [41] but not for the equiatomic CoCrMnNi alloy (Fe0) nor any of the non-equiatomic alloys in our pseudo-binary system that lie between these two extremes. The Hall-Petch strengthening of the present alloys is estimated in Table I-4 using the values for CoFeMnNi [41]. It is important to note that recent experiments found that twin boundaries also provide effective barriers to dislocations and should be included in Hall-Petch type strengthening estimates

[42]. The crystallite size reported in Table I-4 includes twin boundaries and is used for this purpose. Additionally, the constants determined for CoFeMnNi were measured considering twin boundaries [41]. It is also likely that the locking parameter, k, is compositionally dependent in these alloys as reported in similar HEAs [41, 42]. Without data for the CoCrMnNi (x = 0) Hall-Petch constants, this chemical dependence will be neglected here and instead will be assumed to be invariant with composition as reported in Table I-4. Within the limits of these assumptions, the solid solution strengthening, σ_o, of these alloys linearly increases with increasing Cr content, shown Figure I-8.

In addition to the various strengthening mechanisms mentioned earlier, the chemical dependence of the shear modulus, μ, should be considered. The shear modulus contributes to the force required to move dislocations and thus affects the strength of alloys [22]. Table I-5 lists the room temperature elastic constants measured by RUS. There is a weak, nonlinear, relationship between the Cr/Fe content of these alloys and the shear modulus, as shown in Figure I-9. To account for this influence, the solid solution strengthening values from Table I-4 are normalized by the shear modulus, and the results are shown in Figure I-10. This figure provides a clear picture of the effects of composition alone on solid solution strengthening.

One way in which composition can affect solid solution strengthening is through changes in the lattice parameter since the lattice can increase/decrease with atomic size (atomic displacement). The effect of composition on lattice parameter was shown previously in Figure I-5. Comparing the normalized solid solution strength with the lattice parameter shows a strong linear relationship in Figure I-11. Therefore, the underlying physical mechanism for the effect of composition is the atomic displacement corresponding to a particular composition. Intuitively, this agrees well with the results reported in Okamoto et al. [33] for equiatomic alloys: the degree of solid solution strengthening scales with changes in atomic displacement. It appears that measuring the lattice parameter or MSAD offers both an easier and more physical approach to understanding the solid solution strengthening in HEAs. Importantly, this scaling appears to be linear and similar trends may be found in other pseudo-binary systems.

Summary

A pseudo-binary MnCoNi-$Cr_{(25-x)}$-$Fe_{(x)}$ HEA series was thermomechanically processed and characterized to understand the compositional dependence of atomic displacement and solid solution strengthening. The lattice parameter was found to serve as an easy-to-measure alternative to directly measuring the MSAD with synchrotron radiation and scales linearly with the Fe/Cr content. This agrees well with previous work that found Cr produced larger atomic displacements in CrMnFeCoNi alloys than Fe, leading to an expansion of the lattice. The solid solution strength was measured by tensile testing and accounting for other strengthening mechanisms. The solid solution strength was found to linearly scale with the lattice parameter offering a physically intuitive model for solid solution strengthening in FCC HEAs based on atomic displacements.

Appendix I

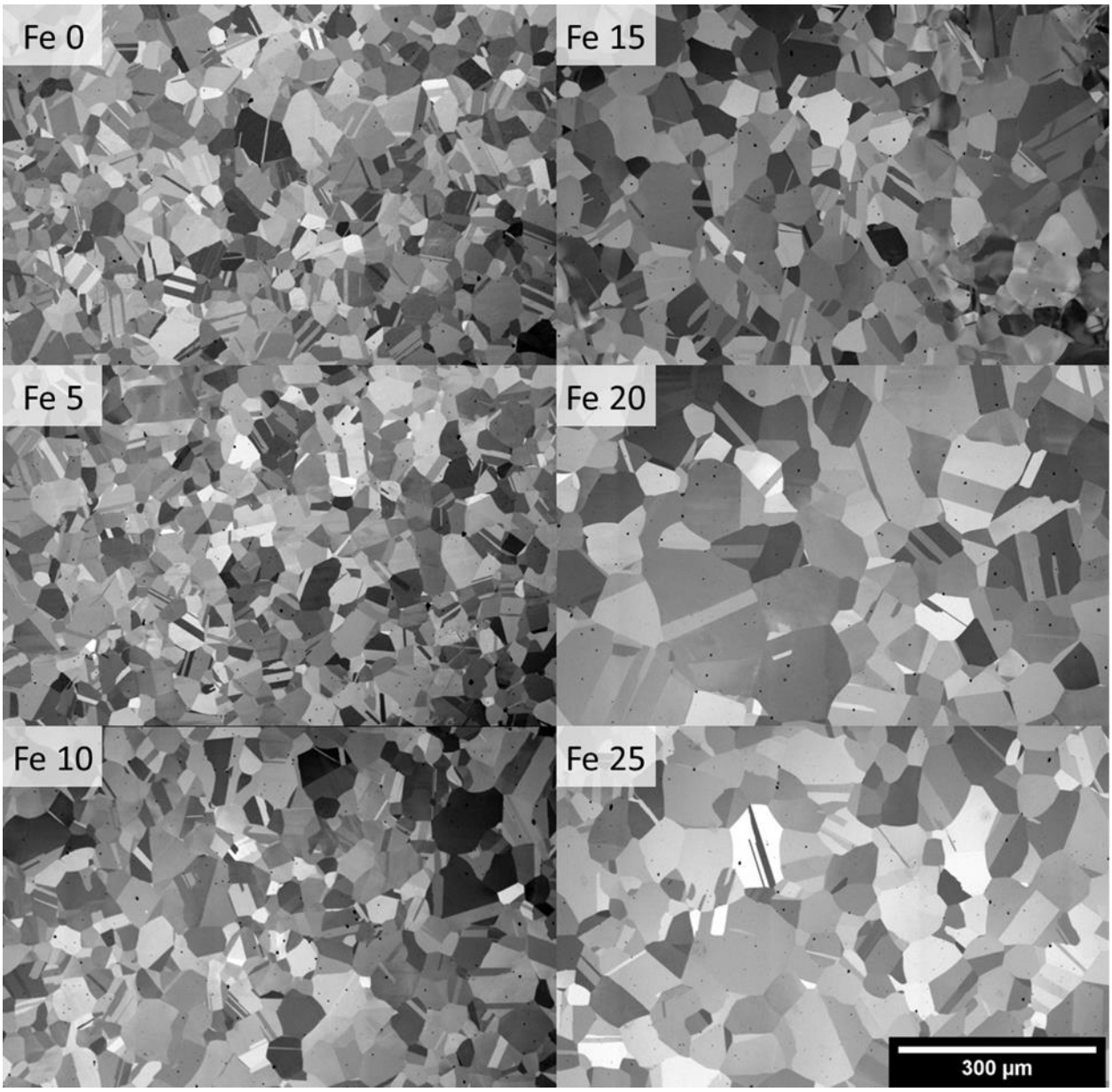

Figure I-1: Representative backscattered electron micrographs of the cold rolled and annealed microstructures. The scattered black particles are Cr-rich oxides formed during melting and casting.

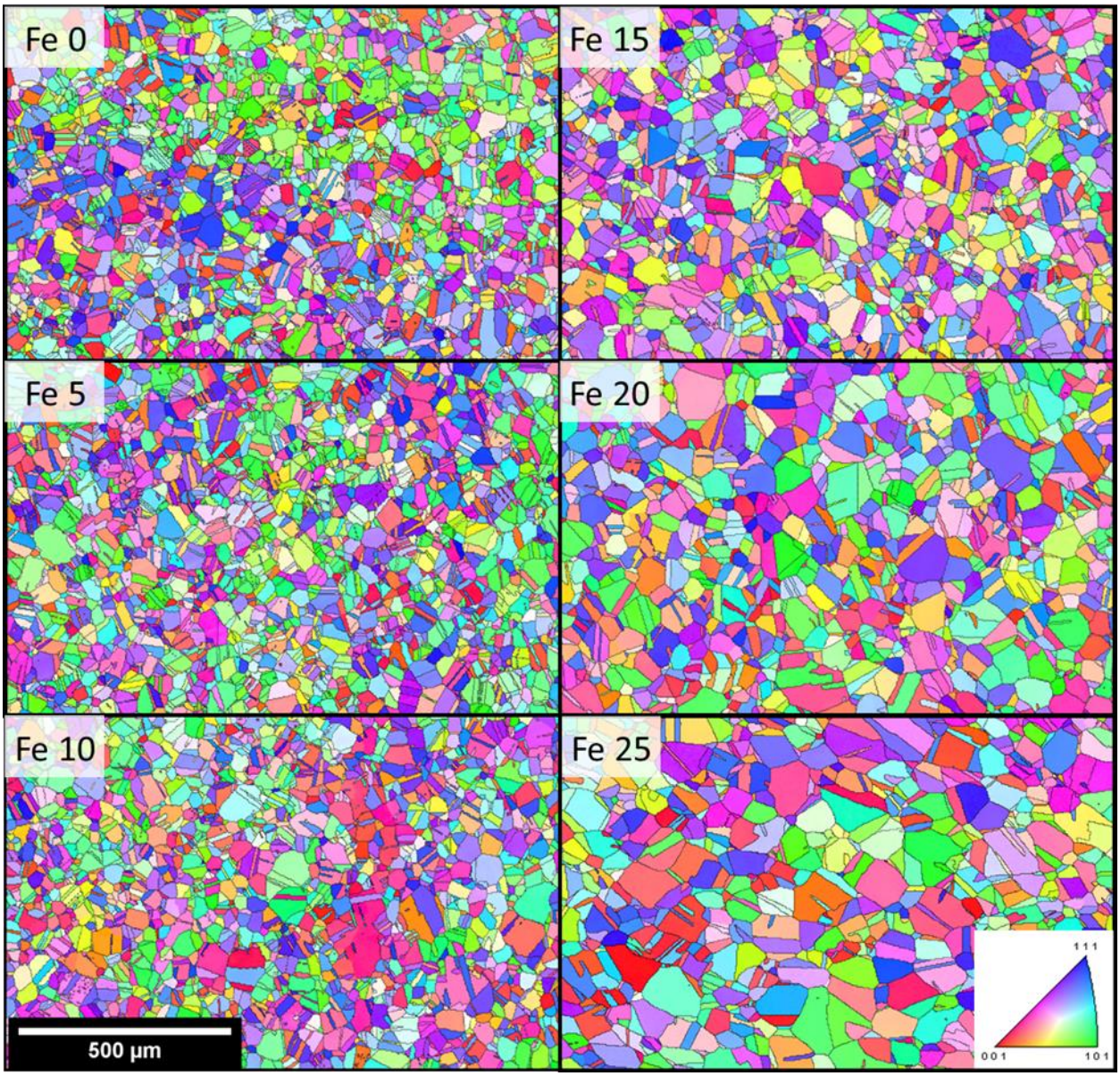

Figure I-2: Inverse pole figure maps depicting the random texture and equiaxed grain structure of the recrystallized samples.

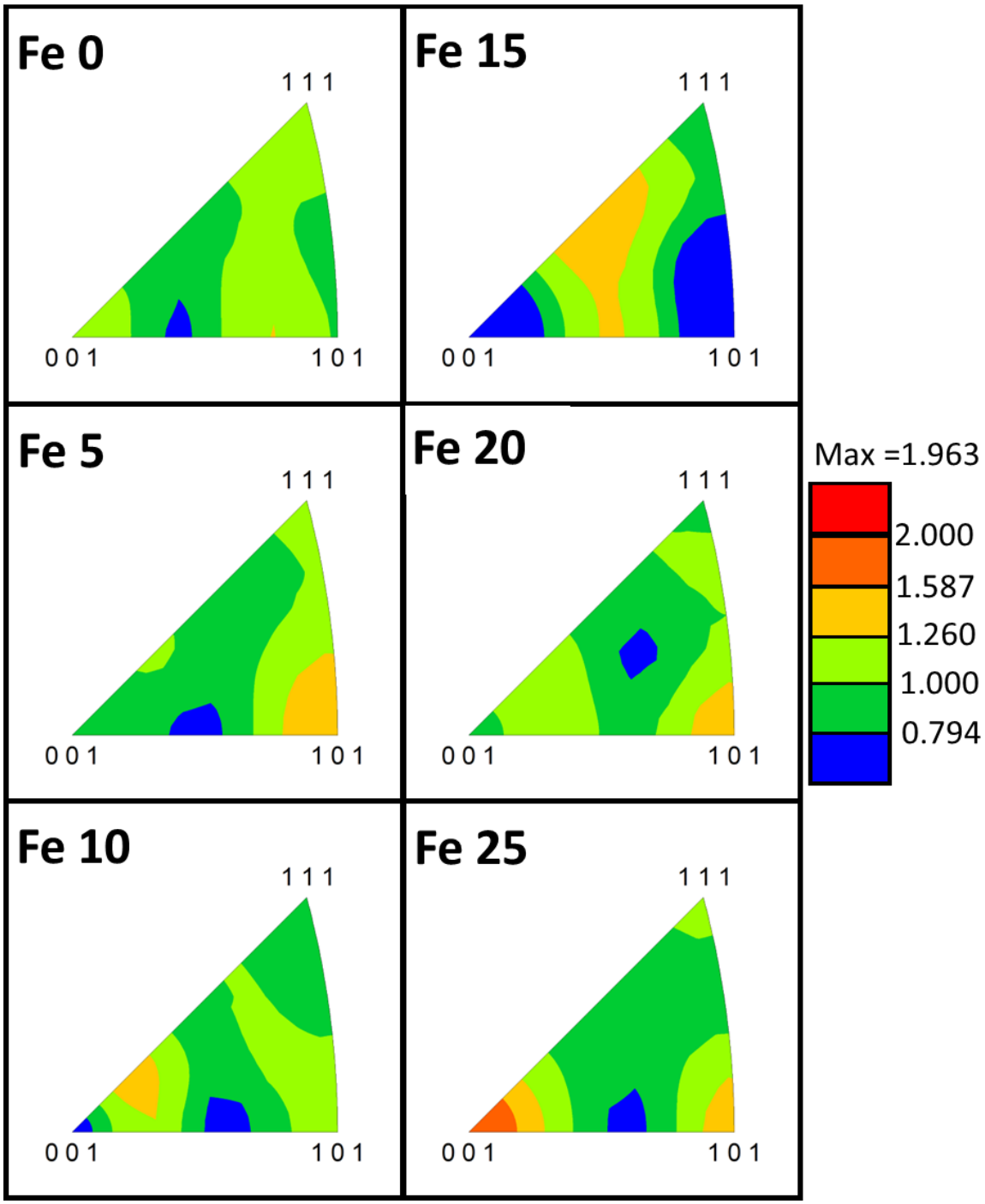

Figure I-3: Inverse pole figures of the regions shown in Figure I-2 depicting the texture as multiples of random orientation.

Table I-1: Grain and crystallite sizes measured by the linear intercept method from the EBSD images acquired in Figure I-2. The crystallite size includes intercepts with annealing twins while the grain size excludes them.

	Grain Size (μm)	**Crystallite Size (μm)**
Fe0	42	22
Fe5	41	22
Fe10	44	25
Fe15	51	29
Fe20	64	37
Fe25	82	47

Table I-2: The composition of each alloy (in at%) as measured by EDS. Values for each alloy may add to over 100% due to rounding errors.

	Co	**Mn**	**Ni**	**Cr**	**Fe**
Fe0	26	25	25	26	0
Fe5	26	25	25	20	5
Fe10	26	25	25	15	10
Fe15	26	25	25	10	15
Fe20	26	24	25	5	20
Fe25	26	24	24	0	26

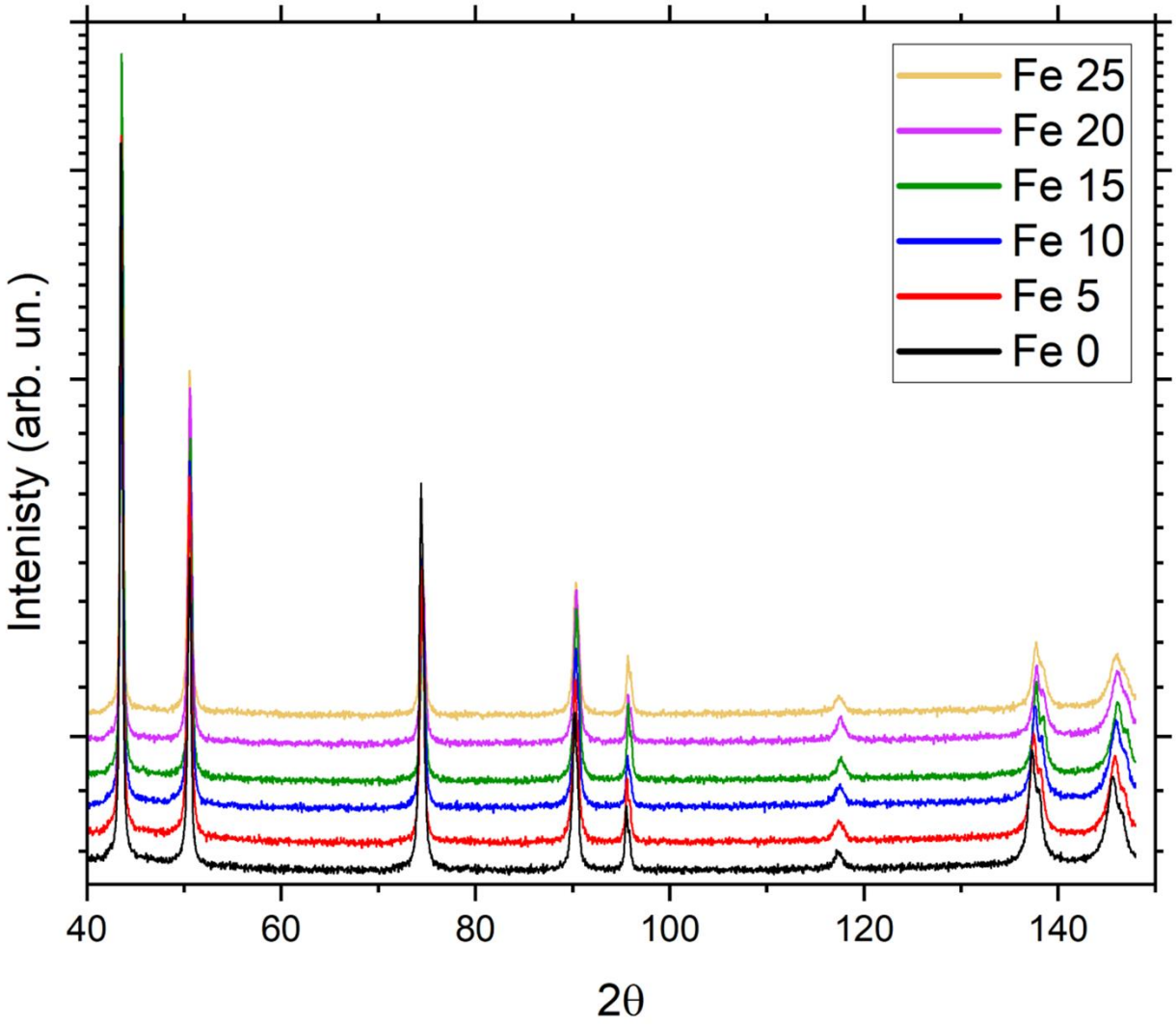

Figure I-4: XRD patterns utilizing Cu Kα radiation. Only FCC reflections are present with peak splitting at higher angles resulting from the Kα1/Kα2 split.

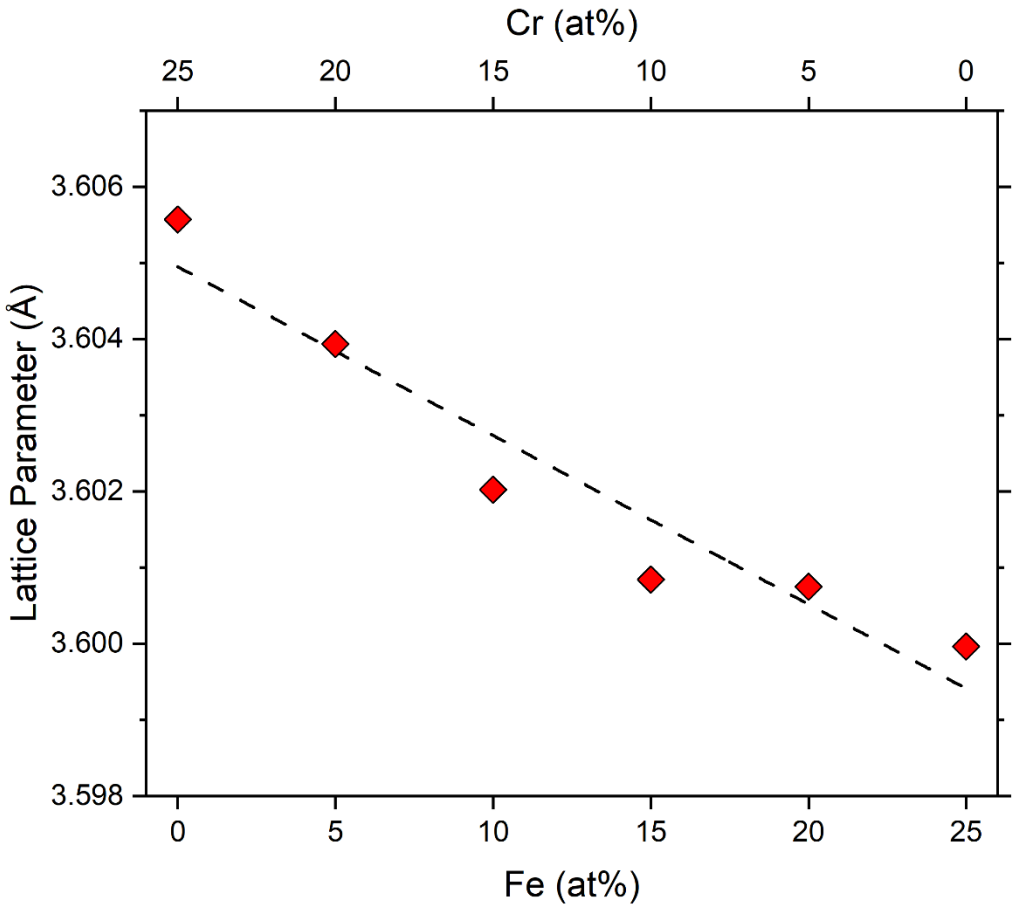

Figure I-5: Lattice parameter as a function of composition in the pseudo-binary $Co_{25}Ni_{25}Mn_{25}Fe_xCr_{25-x}$ system. The lattice parameter was calculated using the Nelson-Riley method [35, 36]. Split peaks were separately fit using Kα1 and Kα2 while non-split peaks use the weighted average. Adjusted $R^2 = 0.900$

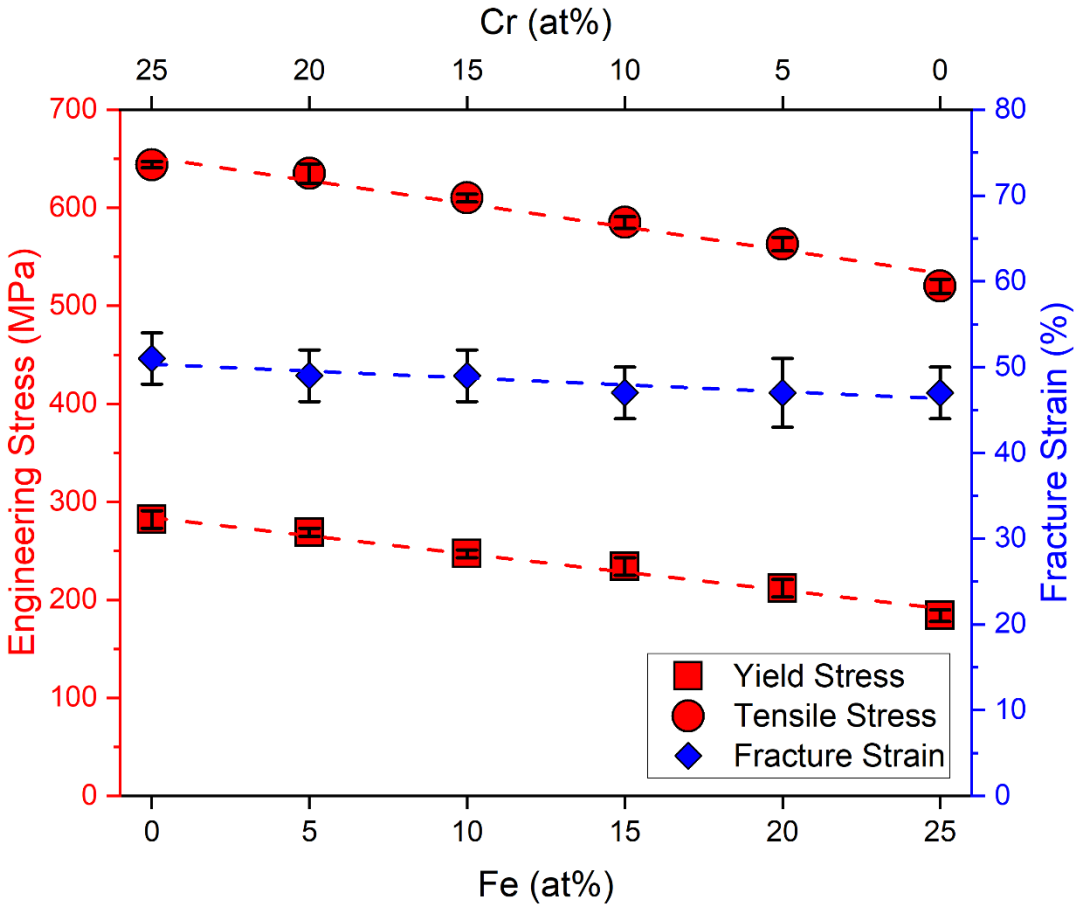

Figure I-6: Tensile properties as a function of composition in the pseudo-binary $Co_{25}Ni_{25}Mn_{25}Fe_xCr_{25-x}$ system. Both yield and tensile stresses decrease with Fe content while elongation to fracture remains roughly constant. Reported uncertainty is ±1 standard deviation of three tensile tests.

Table I-3: A summary of tensile properties. Reported uncertainty is ±1 standard deviation of three tensile tests.

	Yield Stress (MPa)	**Ultimate Tensile Stress (MPa)**	**Uniform Elongation (%)**	**Elongation to Fracture (%)**
Fe0	282 ± 9	644 ± 3	41 ± 3	51 ± 3
Fe5	269 ± 4	635 ± 10	40 ± 1	49 ± 3
Fe10	247 ± 4	610 ± 4	40 ± 2	49 ± 3
Fe15	234 ± 9	585 ± 6	39 ± 2	49 ± 3
Fe20	212 ± 9	563 ± 7	39 ± 2	47 ± 4
Fe25	184 ± 6	520 ± 7	39 ± 2	48 ± 3

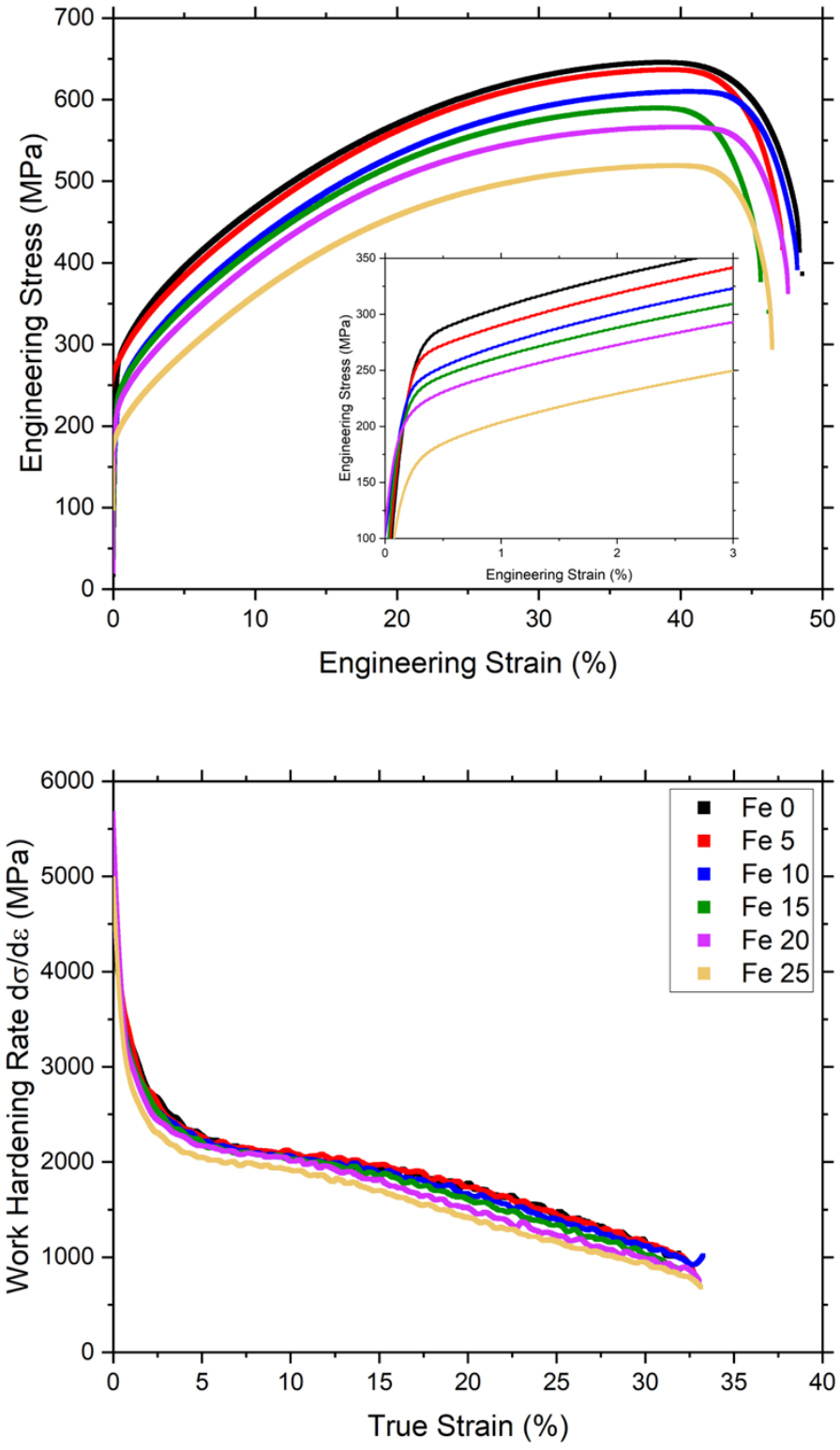

Figure I-7: (Top) Representative engineering stress-strain curves. (Top inset) Close-up of the yield point of representative tensile tests. (Bottom) Representative work hardening rates versus true strain.

Table I-4: Solid solution strength after subtracting the grain size dependent term of the Hall-Petch equation. k = 282 MPa $m^{-1/2}$ from [41]

	Crystallite Size (μm)	$kd^{-1/2}$ (MPa)	Yield Strength (MPa)	Solid Solution Strength (MPa)
Fe0	22	59	282	222
Fe5	22	60	269	209
Fe10	25	57	247	190
Fe15	29	52	234	182
Fe20	37	46	212	165
Fe25	47	41	184	143

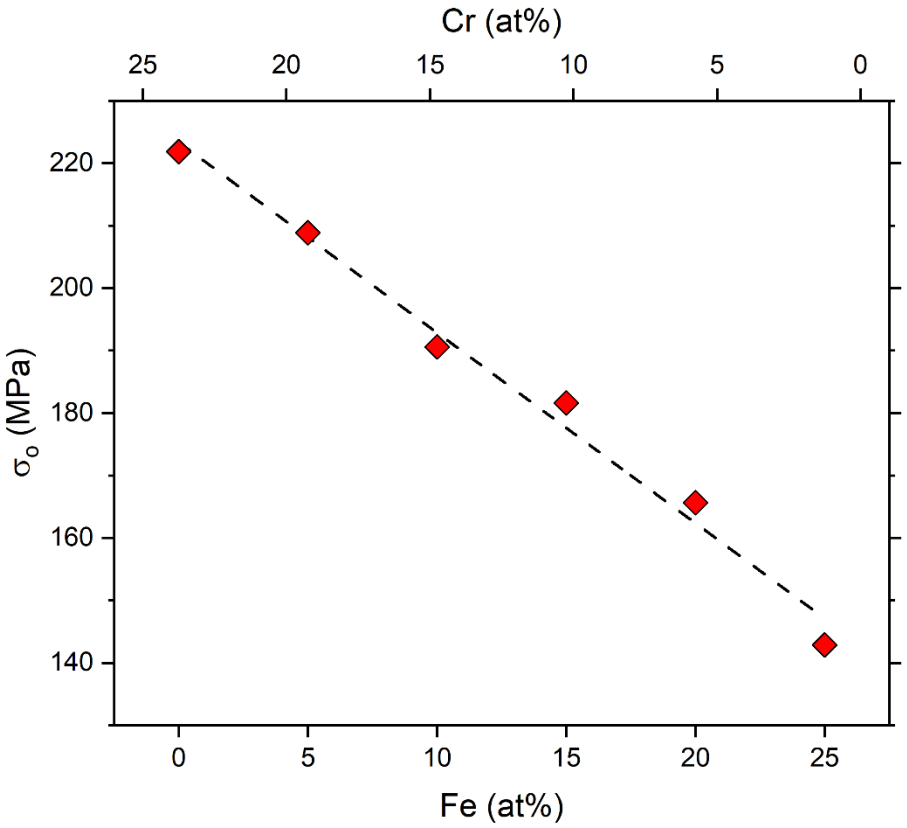

Figure I-8: Solid solution strengthening as a function of composition in the pseudo-binary $Co_{25}Ni_{25}Mn_{25}Fe_xCr_{25-x}$ system. Adjusted R^2 = 0.984

Table I-5: Room temperature elastic constants measured by RUS.

	Shear Modulus, μ (GPa)	Young's Modulus, E (GPa)	Possion's Ratio, ν
Fe0	77	197	0.271
Fe5	79	198	0.262
Fe10	80	199	0.238
Fe15	80	198	0.228
Fe20	79	195	0.233
Fe25	76	190	0.248

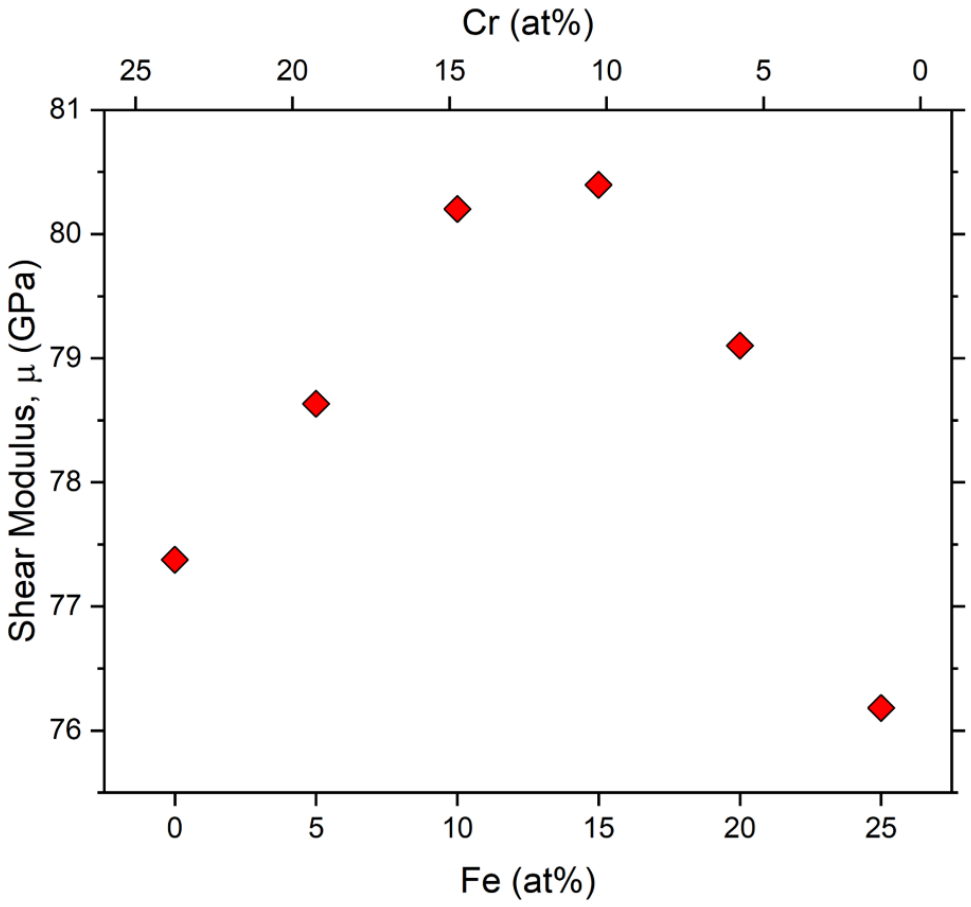

Figure I-9: Shear modulus measured with RUS as a function of composition in the pseudo-binary $Co_{25}Ni_{25}Mn_{25}Fe_xCr_{25-x}$ system.

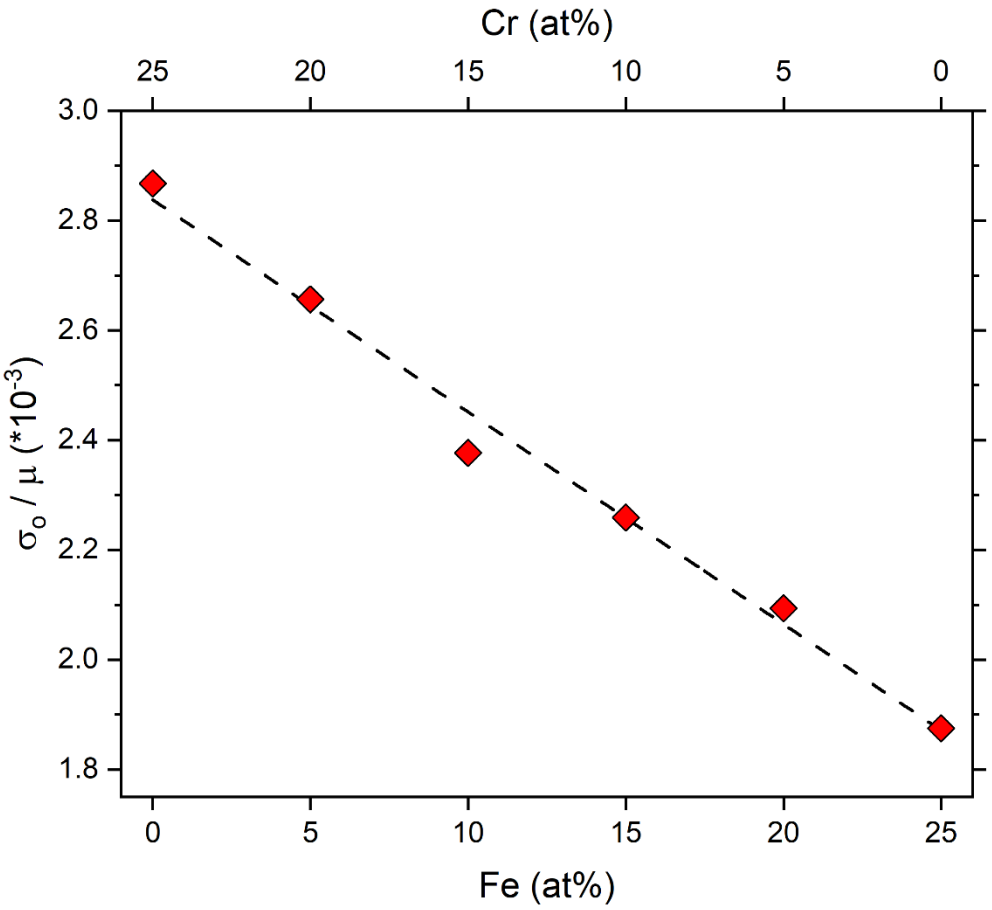

Figure I-10: The solid solution strength normalized with the shear modulus as a function of composition in the pseudo-binary $Co_{25}Ni_{25}Mn_{25}Fe_xCr_{25-x}$ system. Adjusted $R^2 = 0.986$

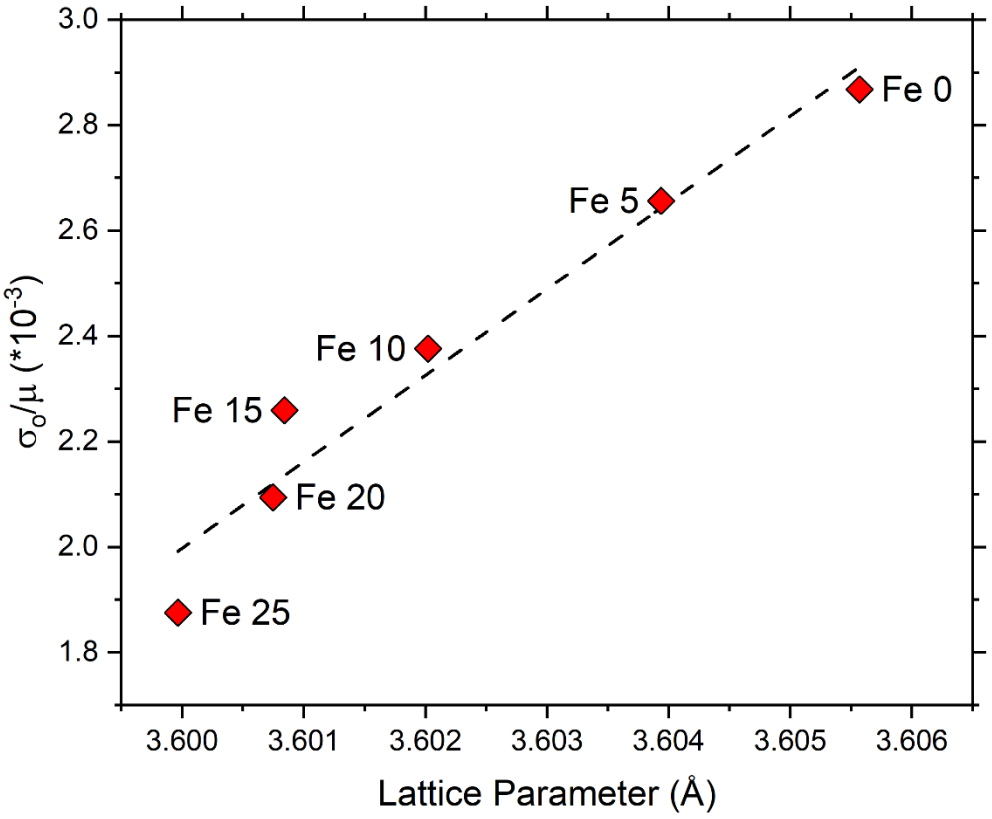

Figure I-11: Normalized solid solution strengthening as a function of lattice parameter in the pseudo-binary $Co_{25}Ni_{25}Mn_{25}Fe_xCr_{25-x}$ system. Adjusted $R^2 = 0.936$

Chapter II
The Compositional Dependence of Transformation-Induced Plasticity (TWIP) in a Pseudo-Binary CrCoNi Alloy System

A version of this chapter is being prepared for publication in a peer-reviewed journal. Josh Cicotte prepared all the cast and thermomechanically processed materials for this study, performed the tensile testing and SEM microscopy, and analyzed all the data. Josh Cicotte wrote and prepared all sections of this chapter. TEM samples were prepared by Gavin Mattingly and Jefferey Baxter at the Oak Ridge National Laboratory. Weicheng Zhong performed the TEM imaging and diffraction. RUS samples were prepared by Ian Stinson and the RUS data were collected and processed by Josh Cicotte. Easo George conceived the study and supervised the project.

Introduction

Deformation-induced twinning is a deformation mechanism that continually introduces new dislocation barriers, twin boundaries, during plastic deformation. This provides a "dynamic Hall-Petch" effect by continually subdividing the grains into smaller regions [43, 44]. This produces the twinning induced plasticity (TWIP) effect which increases both the ductility and strength of alloys [10, 43, 45]. It is well known to occur in FCC alloys, namely Fe-Mn alloys/steels [10, 12, 46-49], some stainless steels [50-53], and several Co-based alloys in the Co-Ni-Cr-Mo systems [45]. The first alloys to make use of TWIP were the Fe-Mn Hadfield steels in the late 1880s, although it wasn't until the 1960s and 70s that deformation twinning was recognized and characterized [54].

The previous work on TWIP alloys has shown that the stacking fault energy (SFE) and critical twinning stress are the fundamental parameters controlling deformation twinning [43]. The SFE is the interfacial energy of the faulted region between two Shockley partial dislocations formed by the disassociation of primary <110> dislocations [50, 55]. Current models for the formation of FCC deformation twins are based upon layered stacking faults, in which, a minimum of three stacking faults on sequential closed packed planes, {111}, results in a twinned region three atomic layers thick [56]. Additional stacking faults can be added, which increase the thickness of the twin [56]. Decreasing the SFE allows the width of the stacking faults, the distance between the partial dislocations, to increase, it also increases the number of stacking faults [49, 50, 55]. Together, they result in increased formation of twins [43]. The formation of twins is orientation dependent and there is a critical stress for twinning, similar to the critical resolved shear stress for slip [56-60]. In polycrystalline materials, once a grain with a favorable Schmid factor reaches the critical resolved twinning stress, deformation twins will begin to form. This critical stress is dependent on the SFE, and a model has been proposed by Steinmetz et al. [58].

The SFE plays a crucial role in deformation twinning and several studies have placed bounds on the SFE between which twinning frequently occurs, ~10-50 mJ/m^2 [10, 45, 49, 51]. For SFEs above this range, alloys tend to only deform by slip, with a limited range where both deformation mechanisms may occur. Alloys with SFEs below this range tend to form HCP martensite instead of deformation twins. There is an intuitive link between very low SFE and the HCP structure: A single intrinsic stacking fault produces a four atomic layer HCP stacking sequence of ABAB and stacking faults on every other atomic layer grows the HCP stacking sequence [61].

While there appears to be a moderate to weak dependence of SFE on temperature, it is primarily controlled through composition [11, 51, 62]. The Fe-Mn system has been studied previously to understand the relationship between SFE, composition, and deformation twinning [10, 11, 48, 49]. Work in Cr-Co-Ni alloys found that increasing the Co concentration lowers the SFE and promotes twinning [45, 63]. Recent focus includes HEAs and the large compositional space they inhabit. There is now extensive evidence of deformation twinning in several FCC

equiatomic high entropy alloys (HEAs), namely in CrMnFeCoNi [59, 64, 65] and CrCoNi [60, 66]. To further investigate the compositional dependencies of deformation twinning in HEAs, a pseudo-binary Cr_{33}-$Co_{(x)}$-$Ni_{(67-x)}$ system was designed to systematically vary the composition and study the resulting mechanical properties (all compositions in at% unless otherwise noted).

Methods

Processing

A pseudo-binary system of alloys with the compositions Cr_{33}-$Co_{(x)}$-$Ni_{(67-x)}$ (all compositions in at%) where x = 1, 10, 20, and 33 were fabricated by are melting the constituent elements (purity >99.99%) into buttons in a water-cooled copper crucible under Ar atmosphere. The buttons were flipped and remelted at least five times to ensure the alloys were thoroughly mixed before drop-casting into a 12.7 mm x 12.7 mm x 76.2 mm rectangular mold. The ingots were encapsulated in evacuated quartz tubes backfilled with Ar and homogenized at 1473 K for 48h. After the homogenization, the capsules were removed from the furnace and broken to allow the alloys to air cool to room temperature. The ingots were longitudinally sectioned along the center line, ground to remove any casting porosity, and cold rolled to 75% reduction. The cold rolled material was annealed at 1173 K for 1h in air and allowed to air cool to produce a fully recrystallized, equiaxed grain structure.

Characterization

X-ray diffraction (XRD) with Cu Kα radiation was used to characterize the microstructure and measure the lattice parameter of each recrystallized alloy. Additionally, backscattered electron (BSE) micrographs were captured to ensure no additional phases were present below the detection limit of XRD. The grain size of each alloy was measured using the linear intercept method on five BSE micrographs.

Transmission electron microscopy (TEM) was employed to detect and image the deformation-induced nanotwins. TEM samples were prepared by focused ion beam (FIB) milling to lift out and thin samples. Samples were lifted from the uniform portion of the gauge in fractured tensile specimens, away from the fracture surface and shoulders. Selected area diffraction (SAD) and dark field imaging were used to characterize deformation twins. Scanning transmission electron microscopy (STEM) was also employed.

Resonant Ultrasound Spectroscopy

To meet the minimum sample size for resonant ultrasound spectroscopy (RUS), additional material was cold rolled to 40% reduction and annealed at 1273 K for 1hr to produce a fully recrystallized bar ~4 mm thick for the Co1, Co10, and Co20 alloys. From this material, parallelepipeds approximately 3 mm x 4 mm x 5 mm were surface ground and cut to produce highly square surfaces free from defects. RUS was performed on these samples at 298 K. Samples were excited at discrete intervals of 10 Hz between 200 kHz and 1000 kHz. More than 40 resonances were measured and used to calculate the elastic constants. The root-mean-square error of each fit was less than 0.5%.

Tensile Testing

Tensile tests were performed to measure the mechanical properties of each alloy at room (298 K) and liquid nitrogen (77 K) temperatures. Tensile bars were cut from recrystallized material

using wire electrical discharge machining (EDM) with a nominally 7.62 mm x 1.52 mm x 0.76 mm gauge section and polished to 600-grit finish. A constant crosshead displacement rate of 7.62 x 10^{-3} mm s^{-1} provided an engineering strain rate of 10^{-3} s^{-1}. Strain was measured by crosshead displacement and corrected using fiducial markers on the gauge section to remove the machine compliance. The yield stress was measured using the 0.2% strain offset method. Cryogenic tests were performed using a fitted polytetrafluoroethylene (PTFE) cup filled with liquid nitrogen. The tensile bars and grip assembly were allowed to soak for 10 minutes prior to testing to ensure the specimens reached 77K. Liquid nitrogen was continuously added to the bath for the duration of the tests. Three tensile specimens were tested for each condition and composition.

Results and Discussion

Microstructure

The microstructure of each alloy is composed of a single solid solution FCC phase with equiaxed grains. The XRD patterns in Figure II-1 consist solely of FCC reflections. Likewise, the BSE micrographs in Figure II-2 show an equiaxed grain structure with no phase contrast, except for a small volume fraction of dark spherical oxide particles. These particles are below the detection limit of XRD. The grain size, both including and excluding annealing twin boundaries, slightly decreases with increasing Co content, as shown in Table II-1.

Room Temperature Tensile Properties

The room temperature tensile properties are strongly dependent on the Co content and show a steady increase in both ductility and strength as Co is increased up to the equiatomic composition (Co33). Representative engineering stress-strain curves in Figure II-3a show the simultaneous increase in strength and ductility. The shape of the work hardening rate curves, shown in Figure II-3b, are similar for all four alloys with a sharp peak near 1% true strain, followed by a roughly flat and prolonged period of high work hardening. The peak is due to an initial low work hardening for a brief period of ~1% true strain. The work hardening in the flat region after the peak, approximately 10-30% true strain, increases and extends with increasing Co content. All four alloys fail by plastic instability (necking). The increased and prolonged work hardening, delays the strain at which Considere's criterion is met, thereby increasing the uniform elongation [22].

In the equiatomic Co33 alloy, previous work has shown that deformation-induced nanotwinning provides sustained high work hardening [60, 66]. TEM SAD and darkfield imaging were employed to investigate which, if any, of the nonequiatomic alloys in the present study form nanotwins during deformation. Figure II-4 shows deformation-induced nanotwins observed after fracture in Co20. No nanotwins were observed in the Co10 or Co1 alloys after fracture at room temperature. Several measurements and calculations show that Co plays a predominant role in the SFE of CrCoNi alloys: as the Co content is increased the SFE decreases [45, 63, 67]. Therefore, it is reasonable to assume that decreasing the Co content in the present alloys, raises the SFE and increases the difficulty of deformation twinning. Raising the SFE increases the critical twinning stress and delays deformation twinning to higher strains. The true critical twinning stress of the equiatomic CrCoNi (Co33) has been reported as 790MPa ± 100MPa by Laplanche et al. [60] All four alloys surpass this threshold at room temperature and the lack of twinning in Co10 and Co1 strongly suggests that the critical stress is compositionally dependent and increases with decreasing Co content. Further work is required to measure the critical twinning stresses in these alloys and its quantitative dependence on SFE and composition.

In addition to the influence of Co on SFE, there is a chemical dependence of the elastic constants. The shear modulus is of particular interest and is a key parameter in many strengthening and dislocation models [22, 55]. To account for the change in shear modulus with composition on the tensile properties, the shear moduli were measured by RUS and used to normalize the tensile data. The elastic constants are reported in Table II-2. While the normalized tensile curves in Figure II-5a have moved closer in stress to each other, there are still some differences among the alloys, likely from changes in solid solution strength. Similarly, the normalized work hardening rates in Figure II-5b closely resemble one another, with deformation twinning giving Co20 and Co33 slightly higher work hardening rates.

Cryogenic Tensile Properties

The tensile properties of the present alloys were also investigated at liquid nitrogen temperature (77 K) to observe possible changes in deformation mechanisms, in particular whether nanotwinning can be activated in the Co1 and Co10 alloys at cryogenic temperatures [59, 60, 64, 65]. The engineering stress-strain curves measured at 77 K, shown in Figure II-6a, exhibit a different trend with Co content than that at 298 K. As the Co content increases the yield and tensile strengths increase, as they do at 298 K, but the elongation remains nearly constant (especially for the Co10, Co20, and Co33 alloys), unlike the steady increase observed for these alloys at 298 K. Similarly, the work hardening rates in Figure II-6b are nearly identical in shape and increase in magnitude with Co content.

The constant elongation with Co content suggests that the deformation mechanisms of all four alloys are similar at 77 K. TEM was again employed to investigate possible deformation-induced nanotwinning. Figure II-7 shows deformation nanotwins in the Co20, Co10, and Co1 samples tensile tested to failure at 77 K. The activation of deformation twinning in Co10 and Co1 at 77 K results from a combination of factors. There is a slight temperature dependence of SFE which decreases with decreasing temperature. This makes twinning easier by lowering the critical twinning stress. Additionally, shear moduli generally increase with decreasing temperature [22]. This results in increased flow stresses and allows the critical twinning stress to be reached at lower strains.

Differences in Tensile Properties between 298 K and 77 K

To account for the temperature dependence of the shear modulus on the tensile properties, the room temperature shear moduli were extrapolated to 77 K using the empirical method proposed by Varshni [68] and using the constants reported by Laplanche et al. [69], and the results are reported in Table II-3. Like the normalized room temperature tensile curves, the curves measured at 77 K and normalized by the shear moduli, shown in Figure II-8 become closer together but some differences remain. Figure II-9 compares the work hardening rates and true stress-strain curves at 298 K and 77 K. The strength and ductility are significantly increased as twinning is activated in the Co1 and Co10 samples and likely begins earlier in Co20 and Co33 by reaching the critical twinning stress sooner. Laplanche et al. observed this phenomenon in the equiatomic Co33 alloy: decreasing the temperature from 298 K to 77 K reduced the strain at which twinning starts [60].

Figure II-10 compares the normalized work hardening rates and true stress-strain curves, which removes the temperature dependence of the shear moduli. Nevertheless, the large increase in strength with decreasing temperature remains. Wu et al. reported the temperature dependence of the yield strength of the equiatomic CoCrNi alloy and attributed its temperature dependence to Peierls-barrier-dominated lattice friction [8]. It is believed that some amount of plastic flow is

required for deformation twinning to begin so it is unlikely for the nanotwinning to play a role in the yield stress here [43, 56, 58]. Additionally, there is a clear change in the work hardening rate between 298 K and 77 K that can be attributed to nanotwinning. Figure II-10 shows the extension of the linear portion of the work hardening rate to larger true strains at 77 K, which delays necking and increases the ductility. Further, the increase in sustained work hardening rate between 298 K and 77 K is compositionally dependent and Figure II-11 plots the increase in uniform true strain (between 298 K and 77 K) as a function of composition. The equiatomic alloy, Co33, shows the smallest increase in ductility (~5% true strain) with decrease in temperature; this increase in ductility linearly increases with Co content to a maximum in Co1 of ~18% true strain. Co1 and Co10 experience relatively large increases in sustained work hardening as nanotwinning is activated. The increase in ductility observed in Co20 is likely similar to the mechanisms described above for the activation of nanotwinning in Co1 and Co10; the increase in flow stress at 77 K allows the critical twinning stress to be met at lower strains during tensile deformation and therefore provides additional sustained work hardening. The same is likely true of Co33 but diminishing returns set in. Co33 was previously shown to already twin at relatively low strains between approximately 10% and 13% true strain at room temperature. Shifting the onset of twinning to even lower strains between 4% and 7% at 77K offers only a slight increase in the period of sustained work hardening resulting in a smaller relative increase in ductility [60]. The identical elongations and the compositional dependence of the TWIP effect shown in Figure II-11 suggests that the kinetics of the nanotwin formation plays a significant role in the work hardening and ductility of these alloys. Future studies to elucidate the twinning kinetics are strongly recommended.

Summary

A pseudo-binary Cr-Co-Ni system with compositions of Cr_{33}-$Co_{(x)}$-$Ni_{(67-x)}$ where x = 1, 10, 20, 33% were fabricated by arc melting and casting, followed by cold rolling and annealing to produce a single solid solution phase with equiaxed grain structure. Tensile testing at 298 K and 77 K coupled with TEM and RUS lead to the following conclusions. The normalized tensile curves at 298 K show very similar strengths with a minor dependence on Co, likely resulting from solid solution strengthening. The ductility, however, increases rapidly with Co content. The activation of nanotwinning at higher Co contents provides *prolonged* work hardening which delays plastic instability. This allows for greater ductility and a higher tensile strength. At 77 K, the strength exhibits a dependence on Co content like at 298 K and is similarly explained. The ductility at 77 K is independent of composition despite the compositional dependence of SFE. All four alloys exhibit deformation induced nanotwinning. Compared to 298 K, testing at 77 K simultaneously increases strength and ductility for all the alloys investigated here. The increase in strength does not result from the temperature dependence of the shear modulus. The activation/enhancement of deformation nanotwinning provides increased and prolonged work hardening at 77 K allowing for both increased tensile strength and ductility. The improvement in ductility is compositionally dependent and substantially increases in Co1 while Co33 exhibited only a mild increase in ductility. Further studies to understand the SFE and critical twinning stresses as well as the kinetics of nanotwin formation in these alloys are strongly suggested.

Appendix II

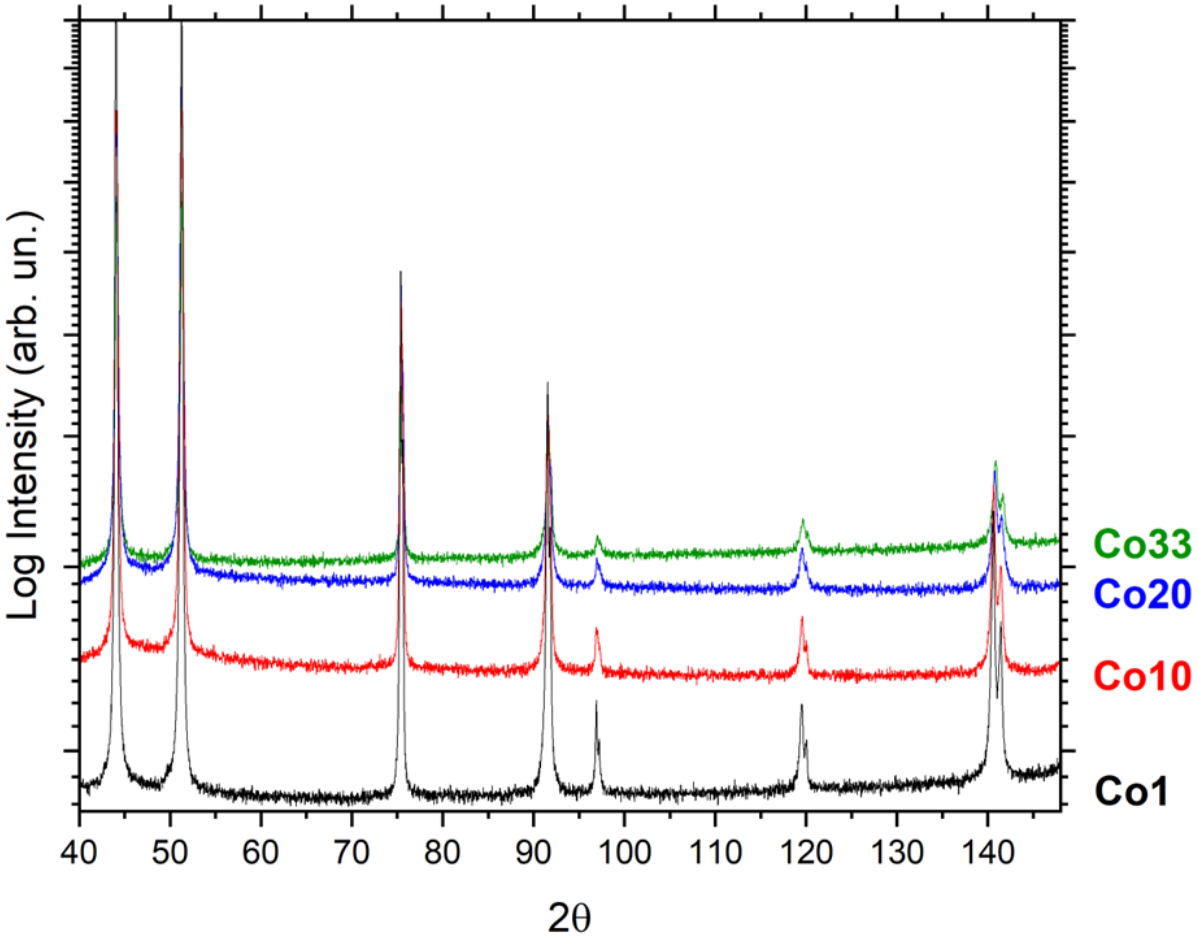

Figure II-1: XRD patterns of cold-rolled and recrystallized alloys in the Cr_{33}-$Co_{(x)}$-$Ni_{(67-x)}$ pseudo-binary system. All reflections are from the FCC solid solution phase.

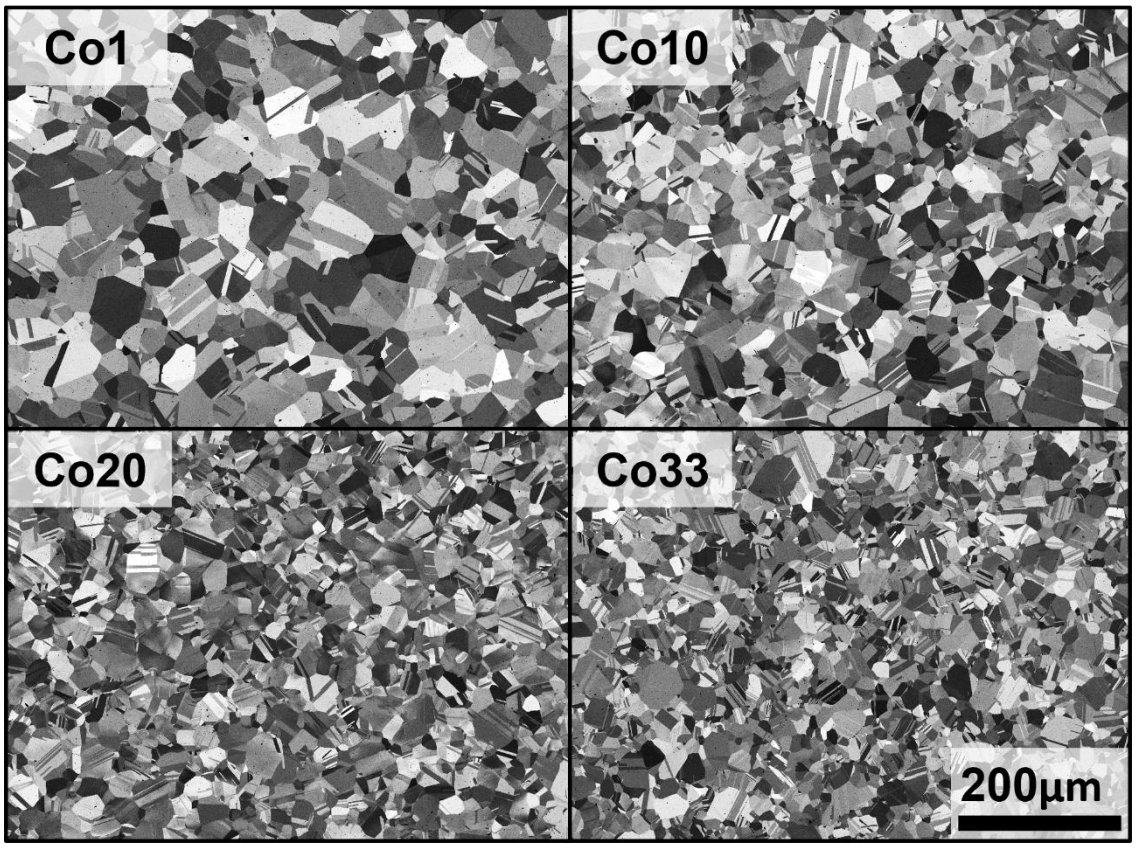

Figure II-2: BSE micrographs showing the fully recrystallized, equiaxed grain structure of alloys in the Cr_{33}-$Co_{(x)}$-$Ni_{(67-x)}$ pseudo-binary system. The small black particles are Cr-oxide inclusions.

Table II-1: Grain size and crystallite size measured by linear intercept method on BSE micrographs. The grain size and crystallite size exclude and include annealing twin boundaries respectively.

	Grain Size, d (µm)	**Crystallite Size, c (µm)**
Co1	33	21
Co10	26	18
Co20	26	14
Co33	21	10

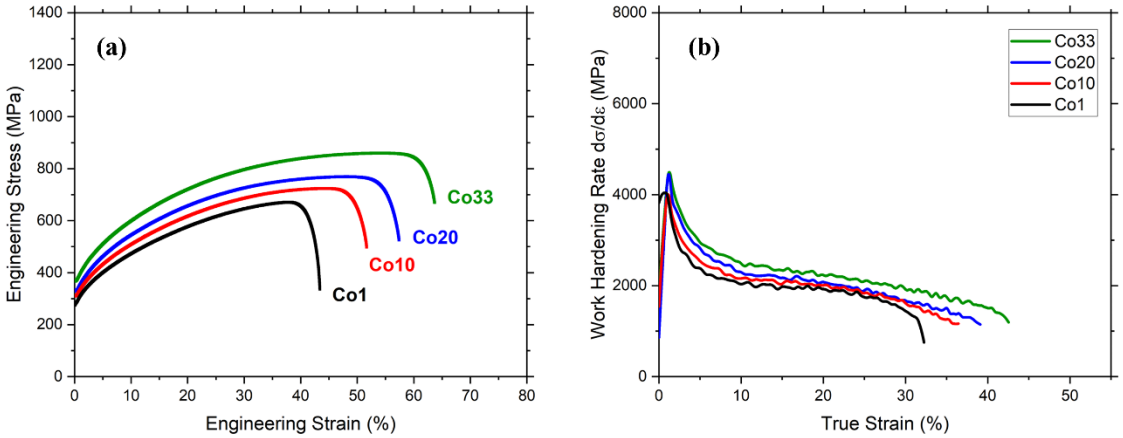

Figure II-3: (a) Representative engineering stress-strain curves of the room temperature tensile properties of the investigated alloys in the Cr_{33}-$Co_{(x)}$-$Ni_{(67-x)}$ pseudo-binary system. (b) Representative work hardening rates as a function of true strain.

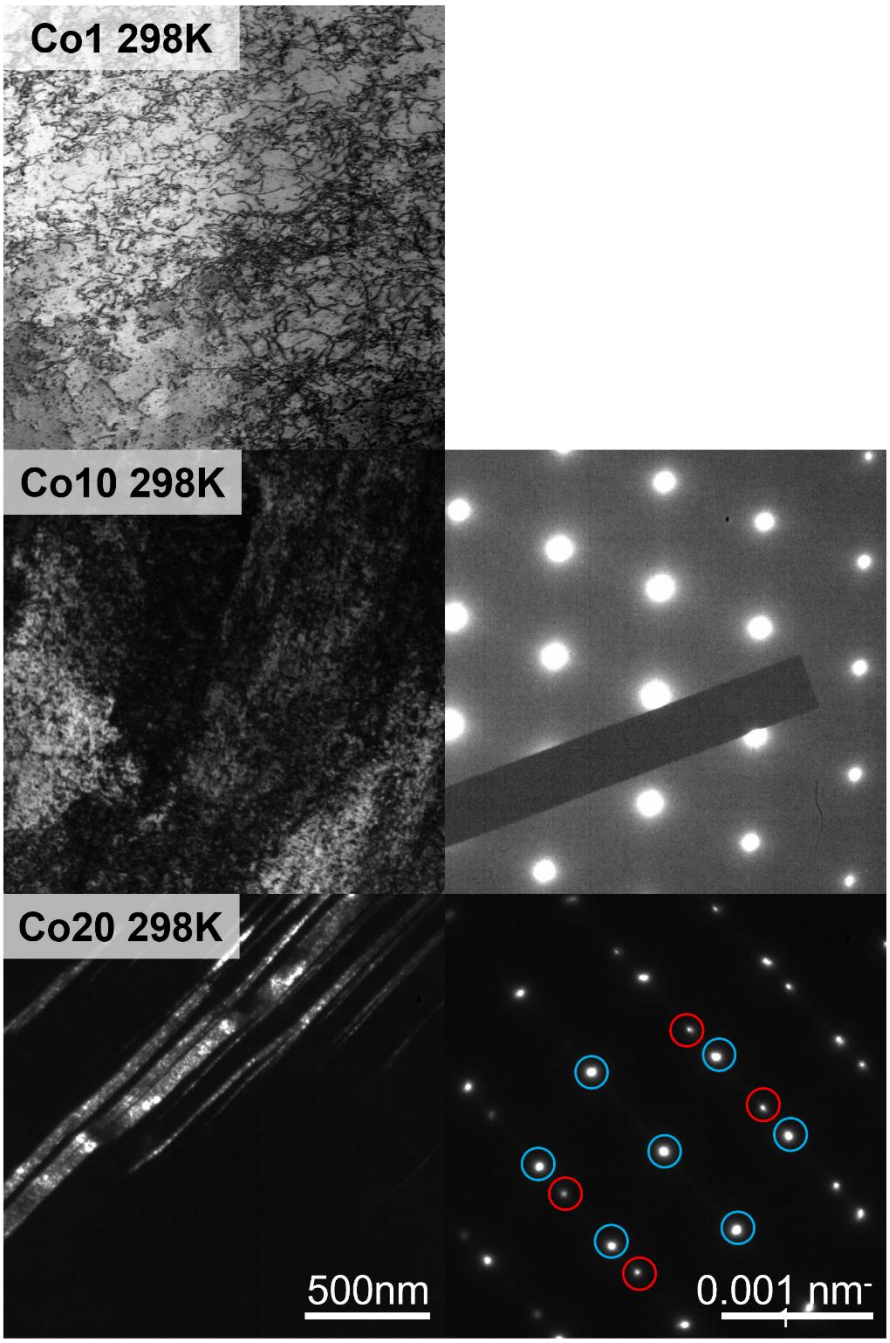

Figure II-4: (Top left) STEM image from the gauge section of a Co1 tensile specimen tested to fracture at 298 K. The image shows a high density of tangled dislocations but no deformation twins were detected. Dark field images (left column) and SAD patterns (right column), from the gauge section of Co10 and Co20 tensile specimens tested to fracture at 298 K. No deformation twins were detected in the Co10 sample and the dark field image was collected using a primary FCC reflection. The dark field image of Co20 shows several deformation-induced twins, imaged using a secondary reflection from the SAD pattern. Blue circles indicate FCC matrix reflections, red circles indicate twinned secondary reflections.

Table II-2: Room temperature elastic constants measured by RUS. *Co33 elastic constants are from [69]

	Shear Modulus, μ (GPa)	**Elastic Modulus, E (GPa)**	**Possion's Ratio, ν**
Co1	83.4	218	0.308
Co10	84.9	221	0.303
Co20	86.6	225	0.297
Co33*	90	235	0.31

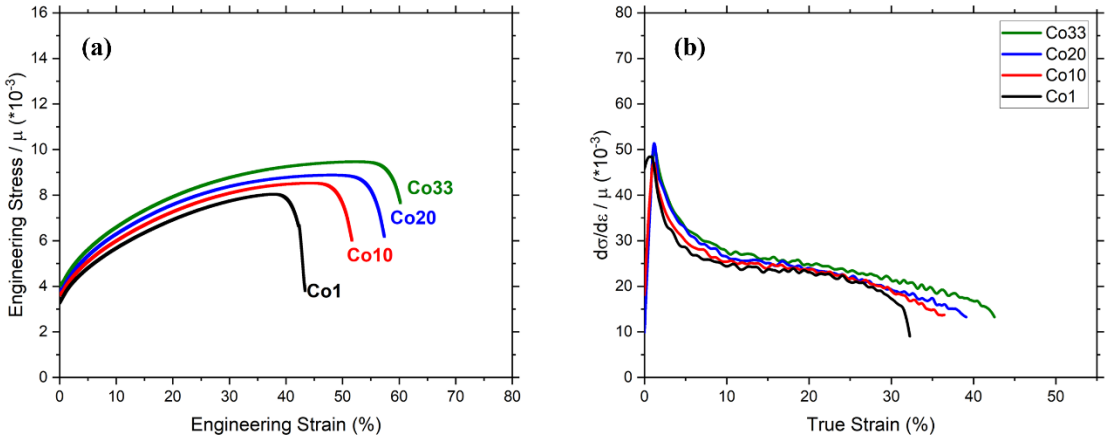

Figure II-5:(a) Tensile curves from Figure II-3 normalized by the shear modulus (b) Corresponding work hardening rates normalized by the shear modulus.

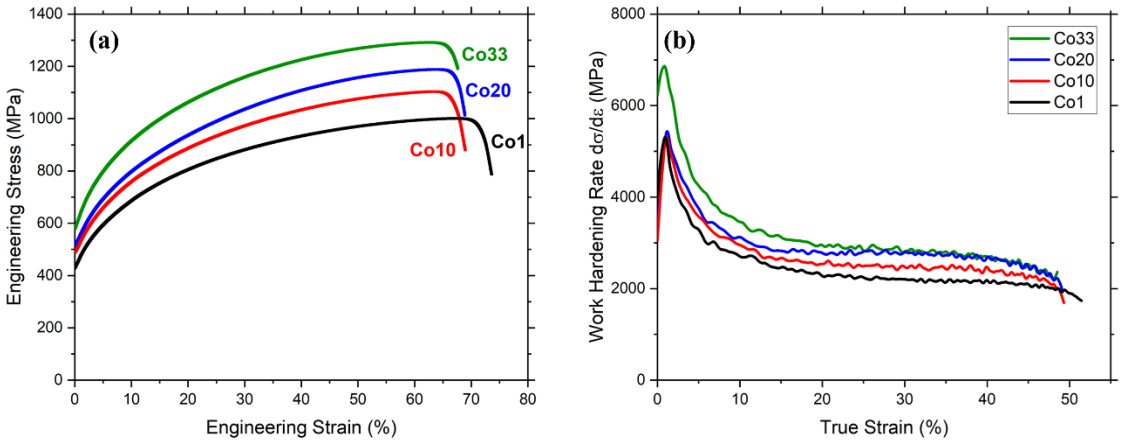

Figure II-6: (a) Representative engineering stress-strain curves measured at 77 K. (b) Corresponding work hardening rates as a function of true strain.

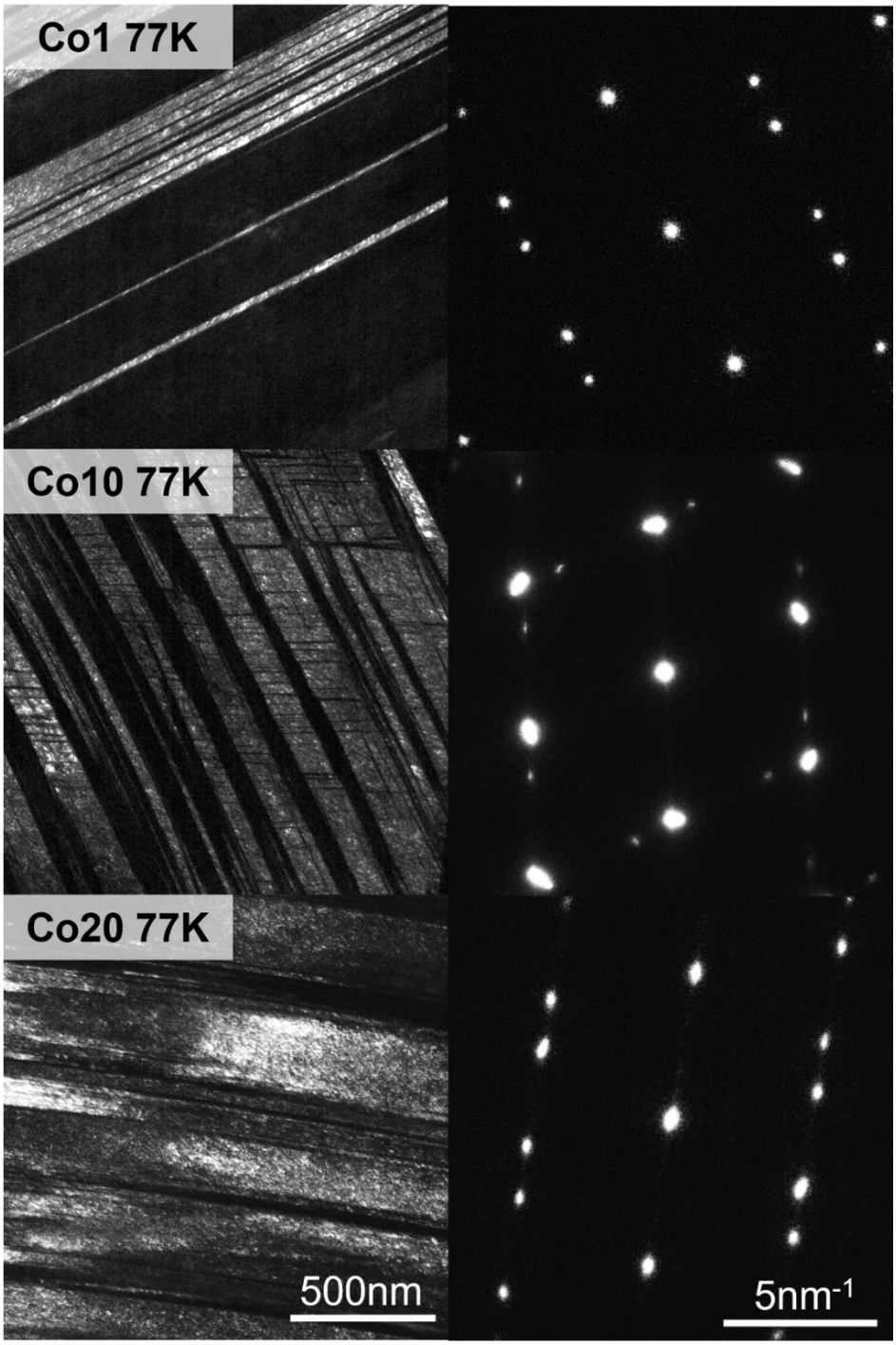

Figure II-7: Dark field images (left column) and SAD patterns (right column) taken from the gauge section of tensile bars tested to fracture at 77 K. Co1, Co10, and Co20 contain a large number of deformation twins. Co10 displays deformation twins formed in two different orientations. The dark field image was collected using a primary reflection, highlighting the matrix. Two distinct orientations can be seen.

Table II-3: Elastic constants extrapolated to 77 K using the 298 K RUS results obtained in the present study and the empirical equation proposed by Varshni [68] with fitting constants taken from Laplanche et al. [69]. The Co33 (equiatomic CrCoNi) constants were used for each alloy.

	Shear Modulus, μ (GPa)	**Elastic Modulus, E (GPa)**	**Possion's Ratio, ν**
Co1	88.3	231	0.309
Co10	89.8	234	0.304
Co20	91.5	238	0.302
Co33	94	245	0.31

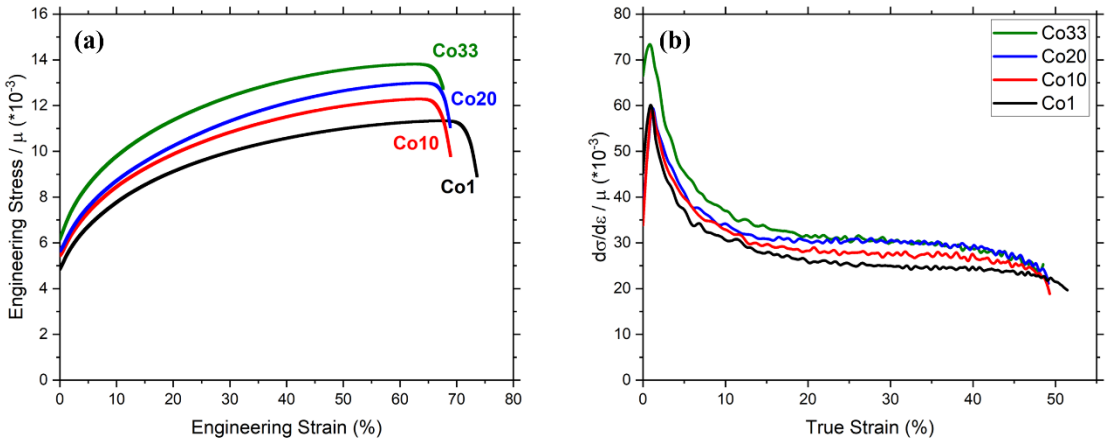

Figure II-8: (a) Tensile curves from Figure II-6 normalized by the shear modulus at 77 K (b) Corresponding work hardening rates normalized by the shear modulus at 77 K.

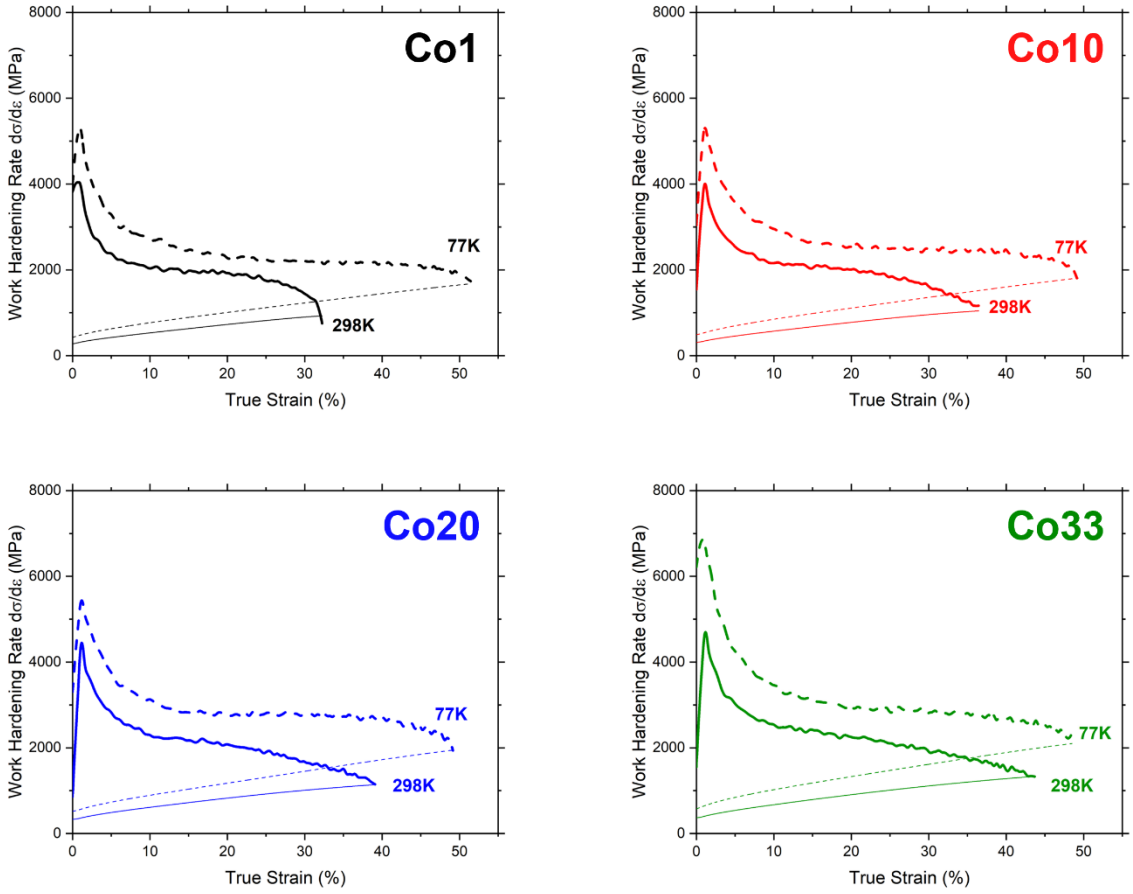

Figure II-9: Work hardening rates as a function of true strain (bold lines) and true stress-strain curves (thin lines) measured at 298 K (solid lines) and 77 K (dashed lines).

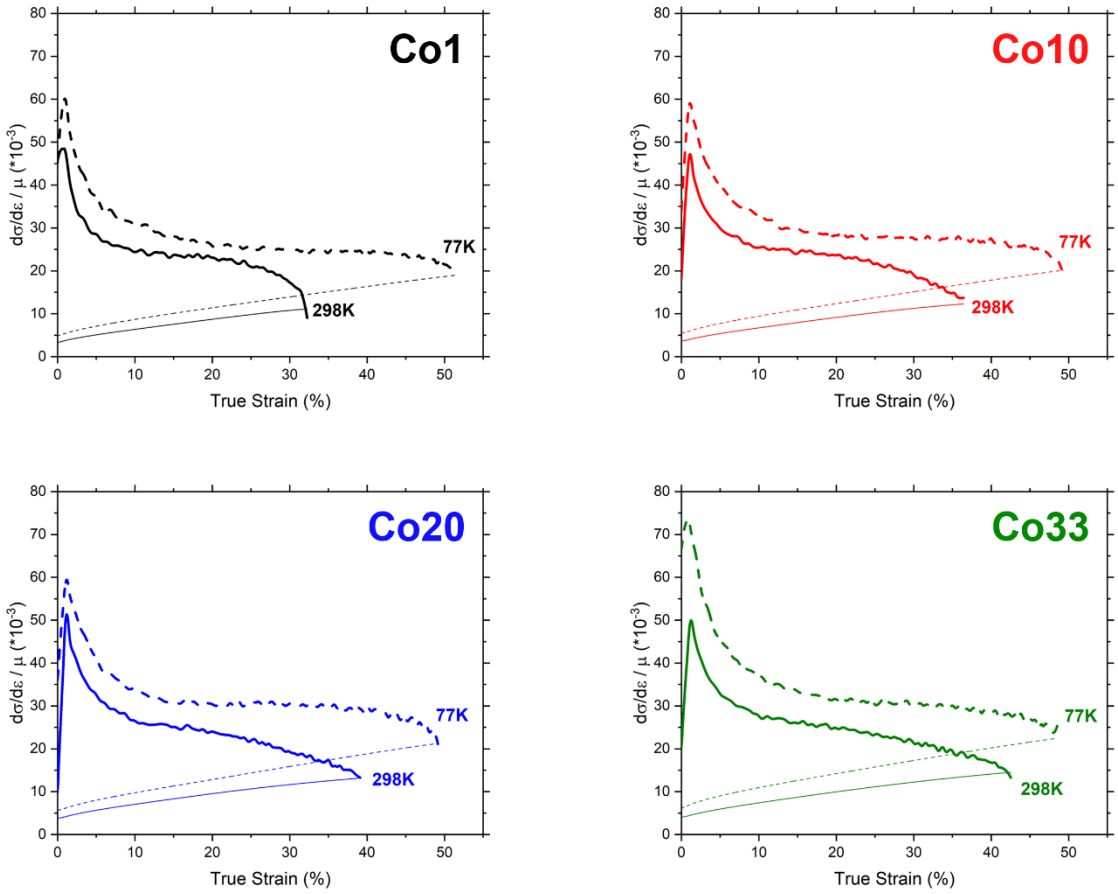

Figure II-10: Work hardening rates as a function of true strain (bold lines) and true stress-strain curves (thin lines) both normalized by their respective shear moduli at 298 K (solid lines) and 77 K (dashed lines).

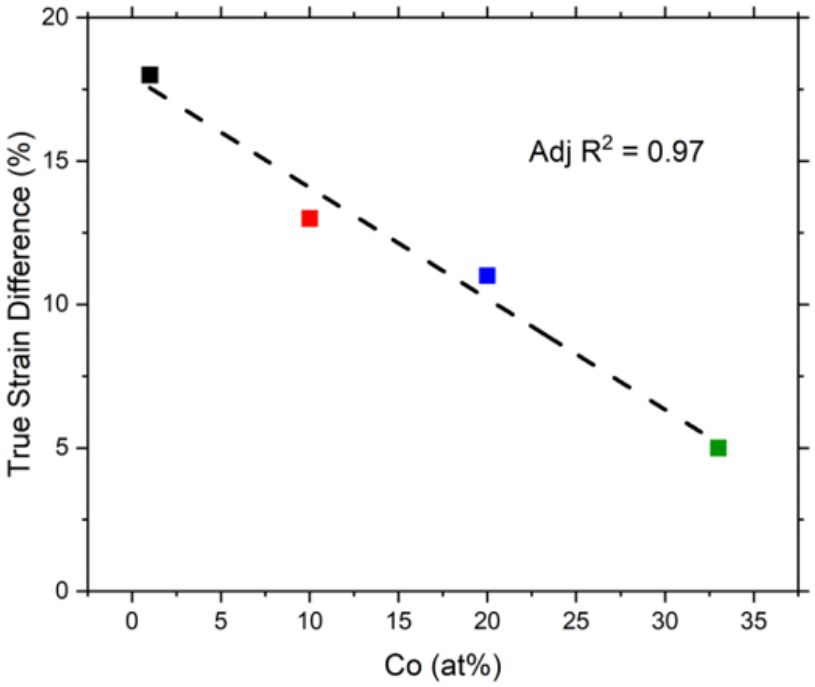

Figure II-11: The difference between the uniform true strain at 298 K and 77 K as a function of Co content. The absolute value of uniform true strain is larger at 77 K in each alloy but the difference in uniform strain decreases with increasing Co concentration.

Chapter III
The Compositional Dependence of Deformation-Induced Martensite in a Pseudo-Binary CrCoNi Alloy System

A version of this chapter is being prepared for publication in a peer-reviewed journal. Josh Cicotte prepared all the cast and thermomechanically processed material for this study, performed the tensile testing and SEM microscopy, and analyzed all data. Josh Cicotte wrote and prepared all sections of this chapter. Dunji Yu and Ke An performed the neutron diffraction experiments at the VULCAN beamline at the Spallation Neutron Source at Oak Ridge National Laboratory. Ying Yang performed the thermodynamic calculations for alloy design. Easo George conceived the study and supervised the project.

Introduction

Transformation induced plasticity (TRIP) has been explored in several traditional FCC alloy systems, namely in Fe alloys (Fe-Mn [10, 12, 46, 70], Fe-Ni [1, 71], various stainless steels [72, 73]) and Co alloys (Co-Cr-Mo [74-77] and Co-Ni-Cr [45]). These alloys form deformation-induced BCC and/or HCP martensites that enable the TRIP effect. The martensite phase boundaries provide significant barriers to dislocation motion and the continued generation of martensite during deformation results in a microstructure refining effect, often termed the "dynamic Hall-Petch effect" [43, 44]. This process of continually subdividing the parent grains with martensite provides increased work hardening rates. Depending on the kinetics of these transformations, very high ultimate tensile strengths or very tough alloys with high ductility can be achieved [12, 46, 78-80].

Recently, TRIP has been investigated in several high entropy alloy (HEA) systems, which offer an increased compositional space compared to traditional single primary element alloys, binary alloys, and dilute ternary systems. The martensitic transformations in FCC HEAs are generally the same HCP [9, 15, 67, 81-85] and BCC [16-19] transformations. However, the increased freedom in composition has allowed for several interesting mechanisms to be studied including a precipitation confining effect [86] (like the confinement offered by fine grains), and a very clear FCC to HCP transformation followed by an HCP to BCC transformation [87]. Several individual HEAs have been designed through thermodynamic modeling [82, 83] to produce TRIP and several relatively small pseudo-binary systems have been investigated [15-19, 81]. Many of these alloys offer good tensile properties but fail to investigate the wide composition spaces afforded by HEAs.

To make use of the wide compositional freedom of HEAs a pseudo-binary Cr_{33}-$Co_{(x)}$-$Ni_{(67-x)}$ alloy system was investigated in this study. The equiatomic CrCoNi alloy undergoes deformation twinning [60, 66], which shares similar mechanisms to the FCC to HCP martensitic transformation [61]. Previous work in Co based alloys has shown that Co reduces the stacking fault energy (SFE) [63, 67] and stabilizes the HCP phase [45]. Additionally, recent calculations of the critical temperature, T_o, (the temperature at which the free energies of the FCC and HCP phases are equal) indicate that it increases with Co concentration in the Cr-Co-Ni ternary system [82]. Here the Co-rich alloys of the pseudo-binary are investigated through tensile testing, neutron diffraction, and electron backscatter diffraction (EBSD).

Methods

Processing

A pseudo-binary system of alloys with the compositions Cr_{33}-$Co_{(x)}$-$Ni_{(67-x)}$ (all compositions are in at% unless otherwise stated) where x = 33, 40, 50, and 57% were fabricated by arc melting the constituent elements (purity >99.99%) into buttons in a water-cooled copper

crucible under Ar atmosphere. The buttons were flipped and remelted at least five times to ensure the alloys were thoroughly mixed prior to drop-casting into a 12.7 mm x 12.7 mm x 76.2 mm rectangular mold. The ingots were encapsulated in evacuated quartz tubes backfilled with Ar and homogenized at 1200 °C for 48h. After homogenization the capsules were removed from the furnace and broken to allow the ingots to air cool to room temperature. The ingots were then heated to 1100 °C and hot rolled to a final thickness of 4 mm for an ~60% reduction. The hot-rolled bars were then annealed to recrystallize any material that did not dynamically recrystallize and ensure a reproducible processing path. The Co33 and Co40 alloys were annealed at 1000 °C for 1h and Co50 and Co57 alloys at 1100 °C for 1h. After both sets of anneals, the alloys, were air cooled to room temperature.

Characterization

Ex-situ neutron diffraction was performed at the Engineering Materials Diffractometer (VULCAN) at the Spallation Neutron Source at Oak Ridge National Laboratory to characterize the volume fraction of FCC and HCP phases before and after tensile testing. Volume fractions were determined by Rietveld refinement of the diffraction patterns using GSAS [88-90].

Electron backscatter diffraction (EBSD) was used to further investigate the microstructure and differentiate between phase and twin boundaries and measure the corresponding grain and crystallite sizes. Further, energy dispersive spectroscopy (EDS) mapping was utilized to distinguish between diffusional and diffusionless transformation product. Backscattered electron (BSE) micrographs were also collected to aid in identifying any additional phases.

Tensile Testing

Tensile specimens for room temperature tensile tests were machined by wire electrical discharge machining (EDM) from the annealed material to produce specimens with a nominally 7.62 mm x 1.52 mm x 1 mm gauge section. Testing was conducted at a constant crosshead displacement rate of 7.62×10^{-3} mm s^{-1} to produce an engineering strain rate of 10^{-3} s^{-1}. Strain was measured by crosshead displacement and corrected using fiducial markers on the gauge section to remove the machine compliance. The yield stress was measured using the 0.2% strain offset method. Three tensile specimens were tested for each composition.

Results and Discussion

Microstructure

In the as annealed condition, Co33, Co40, and Co50 are single phase FCC solid solutions, while Co57 consists of a mixture of FCC and HCP with 23vol% HCP, as shown in the neutron diffraction patterns in Figure III-1.

The EBSD inverse pole figure (IPF) maps in Figure III-2 show each alloy has fully recrystallized and that Co57 has extensive plate-like features after hot rolling and annealing. The phase maps in Figure III-3 reveal that the plate-like features are a mixture of transformed HCP and annealing twins. EDS maps (not shown here for brevity) revealed no chemical composition difference between the FCC and HCP phases, providing evidence that the HCP phase forms in a diffusionless (martensitic) manner. The EBSD maps (Figure III-3) show apparently high amounts of HCP in Co57 and Co50 whereas the neutron diffraction patterns (Figure III-1) indicated no HCP in the Co50 and only 27vol% in Co57. The EBSD results are an artifact due to the near-surface regions undergoing deformation-induced FCC to HCP transformation during specimen

preparation (grinding and polishing). Unlike neutron diffraction, which analyzes deep into the specimens, EBSD samples only the near-surface regions. Therefore, in the present alloys, EBSD is not a reliable way to quantify any phase transformation occurring during tensile testing, for which we use neutron diffraction instead. The IPF maps in Figure III-2 also show that the Co50 and Co57 alloys contain coarser grains than Co33 and Co40 but are of the same order of magnitude. Table III-1 reports the grain size and crystallite size which exclude and include, respectively, twin/phase boundaries. The size of the FCC parent grains in Co57 could not be accurately determined due to the large quantities of surface martensite, however, they appear to be the same order of magnitude as Co50.

Tensile Results

Figure III-4a shows representative engineering stress-strain curves of the different pseudo-binary alloys tested; their tensile properties are tabulated in Table III-2. The yield strength decreases with Co content from Co33 to Co50 before increasing again in Co57. The initial decrease is likely a mixture of decreasing solid solution strengthening, predicted by [34, 82]. Additionally, the substantial increase in grain size from Co40 to Co50 contributes an estimated 40 MPa decrease using the Hall-Petch coefficients provided by Yin et al. for the equiatomic CrCoNi alloy [91]. The increased yield strength of Co57 can be attributed to the thermally transformed martensite, which refines the microstructure. All the alloys, excluding Co50, reach similar ultimate tensile strengths (UTS) between 750 MPa and 800 MPa. The strengthening increments (the difference between UTS and yield strength) are similar across the composition range.

The equatomic Co33 alloy possess the greatest ductility; in the remaining alloys, uniform elongation decreases significantly with increasing Co content, as shown in Figure III-5. The stress-strain curves appear to show necking in each alloy, however, examination of the work hardening rates and true stress-strain curves in Figure III-4b reveals that only the Co33 specimen reaches the Considere's criterion for necking [22]. The other alloys prematurely fracture before necking occurs and the sharp reduction in stress at the end of each tensile curve is due to the propagation of cracks through the tensile specimens. With the exception of Co57, the work hardening rates of the alloys in Figure III-4b are very similar in both shape and magnitude.

Post-Fracture Microstructure

Neutron diffraction of the gauge sections of the fractured tensile specimens revealed significant deformation-induced FCC to HCP transformation in Co40, Co50, and Co57, see Figure III-6. No HCP was detected in the Co33 sample, which is in line with several recent studies which only observed the transformation at temperatures well below room temperature [92, 93]. The relative amounts of each phase were determined by Rietveld refinement of the neutron diffraction patterns and are tabulated in Table III-3. Figure III-7 plots the HCP martensite content before and after tensile deformation, as well as the amount formed during deformation, as a function of composition. The total volume percent of HCP formed after tensile testing increases steadily with the Co content. This agrees well with similar Cr-Co-Ni alloys [45] and intuitively makes sense. Co is HCP at room temperature and increasing its concentration should favor the formation of HCP in the alloy. The amount of deformation-induced martensite, however, peaks in the Co50 sample. The thermally transformed martensite consumes some of the available parent phase in Co57 reducing the amount available to transform by deformation. However, Co57 still retains a large amount of FCC, ~77vol%, prior to tensile testing and fails by fracture before the martensitic transformation can be completed. The nearly total transformation to HCP by polishing, shown by

the phase maps in Figure III-3, suggests that the transformation can in principle occur but the specimen failed in tension prematurely.

Post-fracture IPF and phase maps of Co50 in Figure III-8 show deformation induced HCP plates with a similar morphology to the thermally transformed HCP in Co57 shown in Figure III-2 and Figure III-3. The amount of HCP martensite measured by EBSD closely matches the values determined by neutron diffraction, meaning deformation from polishing introduced little to no additional martensite in this alloy. Additionally, several cracks forming at grain boundaries are highlighted in Figure III-8 in the both the IPF maps and phase maps.

Influence of HCP martensite on tensile properties

Rather than producing the TRIP effect, the deformation induced FCC to HCP transformation significantly reduces the ductility of the present Cr-Co-Ni alloys, as shown in Figure III-9. The uniform elongation decreases linearly with the total fraction of HCP, shown by the best fit line through Co40, Co50, and Co57 (the three alloys which form deformation induced martensite). The Co33 TWIP alloy, possessing no thermal or deformation induced transformation, retains the greatest ductility. The presence of thermally induced martensite does not appear to play a significant role in the ductility of the alloys as Co40 and Co50 both suffer significant reductions in ductility while containing no thermally induced martensite.

Despite the reduction in ductility and the considerable formation of HCP martensite there is little strengthening benefit and no changes in work hardening rate except in Co57. The increased work hardening rate of Co57 is shown in Figure III-4. In-situ diffraction measurements, or a series of ex-situ interrupted tensile tests would be required to fully characterize the transformation kinetics. Using the current data, a link between the true strain and amount of deformation-induced martensite measured at fracture can offer some insight. Figure III-10 shows a clear linear trend in the reduction of ductility as a function of the "transformation rate". The "rate" is defined here as the volume percent of deformation-induced martensite measured at fracture divided by the total uniform true strain, giving an average martensite transformed per true strain.

Remy and Pineau [45] observed similar deleterious effects in Co based alloys with the FCC to HCP martensitic transformation. A marked decrease in ductility and the onset of brittle fracture occurred in alloys tensile tested below the deformation induced transformation temperature (M_d) and above the spontaneous transformation temperature (M_s). The ductility of these alloys was maximized when there were small amounts of transformation product (<10vol%) and quickly dropped as the amount of HCP increased. Amounts greater than 30 vol% lead to premature fracture [45]. Remy and Pineau also investigated several Fe-Mn alloys that transition from TWIP to TRIP (FCC to HCP transformation) with decreasing test temperature [10]. These alloys exhibit a similar peak in ductility just below the M_d temperature and accompanying decrease in ductility with increasing HCP volume fractions. Koyama et al. [94, 95] further investigated the phenomenon in Fe-Mn steels exhibiting this behavior. They identified a plastic incompatibility that exists where HCP plates propagate over existing annealing twin boundaries. The annealing twins lie on close packed planes and are free to deform in the FCC parent phase but the HCP plate that intersects the boundary does so on a non-basal plane, prohibiting slip in the HCP plate. During plastic flow, the resulting incompatibility forms microvoids at these intersections which coalesce and allow for cracks to easily propagate [94]. Lee et al. [96] and Kurosu et al. [97] observed similar fracture mechanisms in Co-Cr-Mo-N alloys that exhibit FCC to HCP deformation-induced transformations.

However, there are two recent HEAs that have shown an advantageous FCC to HCP transformation. Li et al. [9] reported a dual-phase $Fe_{50}Mn_{30}Co_{10}Cr_{10}$ alloy containing ~28 vol% HCP after thermomechanical processing, similar to the Co57 alloy. The Fe-Mn-Co-Cr alloy with fine ~4.5 μm grains contained 84 vol% HCP after tensile testing while reaching a UTS of ~850 MPa and an elongation to fracture of ~75% [9]. This is a similar UTS to the present martensitic alloys but with considerably better ductility. The coarse-grained $Fe_{50}Mn_{30}Co_{10}Cr_{10}$ alloy with ~45 μm grain size can be compared the Co40 alloy which has a grain size of ~50 μm [9]. The UTS and elongation to failure of these alloys are similar, however, the Fe-Mn-Co-Cr alloy starts with some thermally induced HCP and forms considerably more during deformation [9]. The $Fe_{50}Mn_{30}Co_{10}Cr_{10}$ alloy is clearly more tolerant of the FCC to HCP transformation. Additional studies by Li et al. [98, 99] found the HCP phase is relatively ductile in the $Fe_{50}Mn_{30}Co_{10}Cr_{10}$ alloy and appreciably deforms through slip and twinning. No evidence of HCP deformation twinning was found in the present alloys.

Coury et al. [82] investigated a $Co_{55}Cr_{40}Ni_5$ alloy through thermodynamic modeling and in situ synchrotron X-ray diffraction. The alloy is a single-phase FCC solid solution after spray forming and annealing and forms an HCP martensite during deformation. Its grain size is comparable to the present Co33 and Co40 alloys and has a similar true uniform elongation as Co33. However, the $Co_{55}Cr_{40}Ni_5$ alloy work hardens significantly more, reaching an engineering UTS of 950 MPa compared to 800 MPa in Co33 [82]. Additionally, $Co_{55}Cr_{40}Ni_5$ possess far superior ductility to Co57, which possesses a similar composition but larger grain size [82].

The superior mechanical properties of the $Fe_{50}Mn_{30}Co_{10}Cr_{10}$ and $Co_{55}Cr_{40}Ni_5$ alloys are in part likely due to their smaller grain size. Several studies, including additional work on $Fe_{50}Mn_{30}Co_{10}Cr_{10}$, have shown that large grain sizes are generally detrimental to both strength and ductility in FCC to HCP TRIP alloys [85, 99]. Reducing the grain size suppresses the kinetics of transformation, reducing the rate at which HCP martensite is formed as well as the total amount formed [99]. The present pseudo-binary system offers a wide composition range over which TRIP occurs and further work is recommended to refine the grain size and study the transformation kinetics.

Summary

A pseudo-binary high entropy alloy system of $Cr_{33}Co_{(x)}Ni_{(67-x)}$ where x = 33, 40, 50, and 57% was designed to investigate the FCC to HCP TRIP effect in HEAs. The Co40, Co50, and Co57 alloys were all found to undergo the FCC to HCP martensitic transformation and were characterized by neutron diffraction and EBSD. Co33, Co40, and Co50 are single phase FCC solid solutions prior to tensile testing, while the Co57 alloy contains 23 vol% of thermally induced HCP martensite. Tensile testing revealed a strong degradation in ductility with increasing Co content due to the deformation-induced FCC to HCP transformation. Previous work in Co alloys and Fe-Mn alloys found similar deleterious effects of the FCC to HCP transformation. The intrinsic low ductility of HCP structures causes plastic incompatibilities and stress concentrations at annealing twin boundaries and grain boundaries. A few HEAs exhibit a positive TRIP effect from the FCC to HCP transformation but a full understanding of why these alloys avoid the deleterious effects seen in other alloys is lacking. Further work to refine the grain size and understand the transformation kinetics of these alloys is recommended.

Appendix III

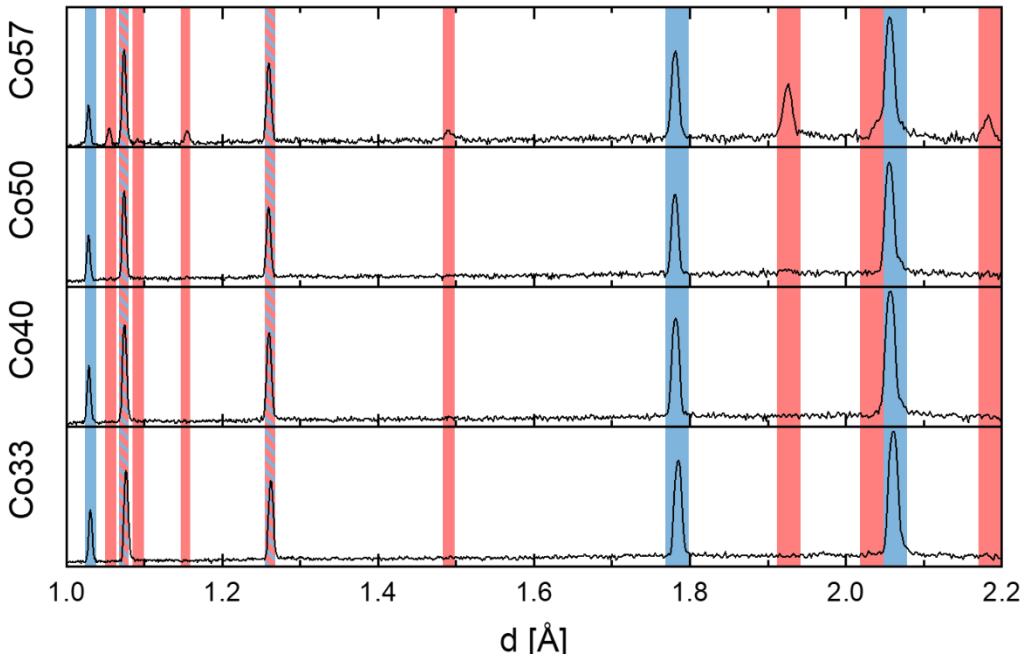

Figure III-1: Neutron diffraction patterns collected from the grip portion of tensile specimens, representing the as annealed microstructure. Red lines indicate HCP reflections and blue lines indicate FCC reflections. The striped bars indicate reflections shared by FCC and HCP.

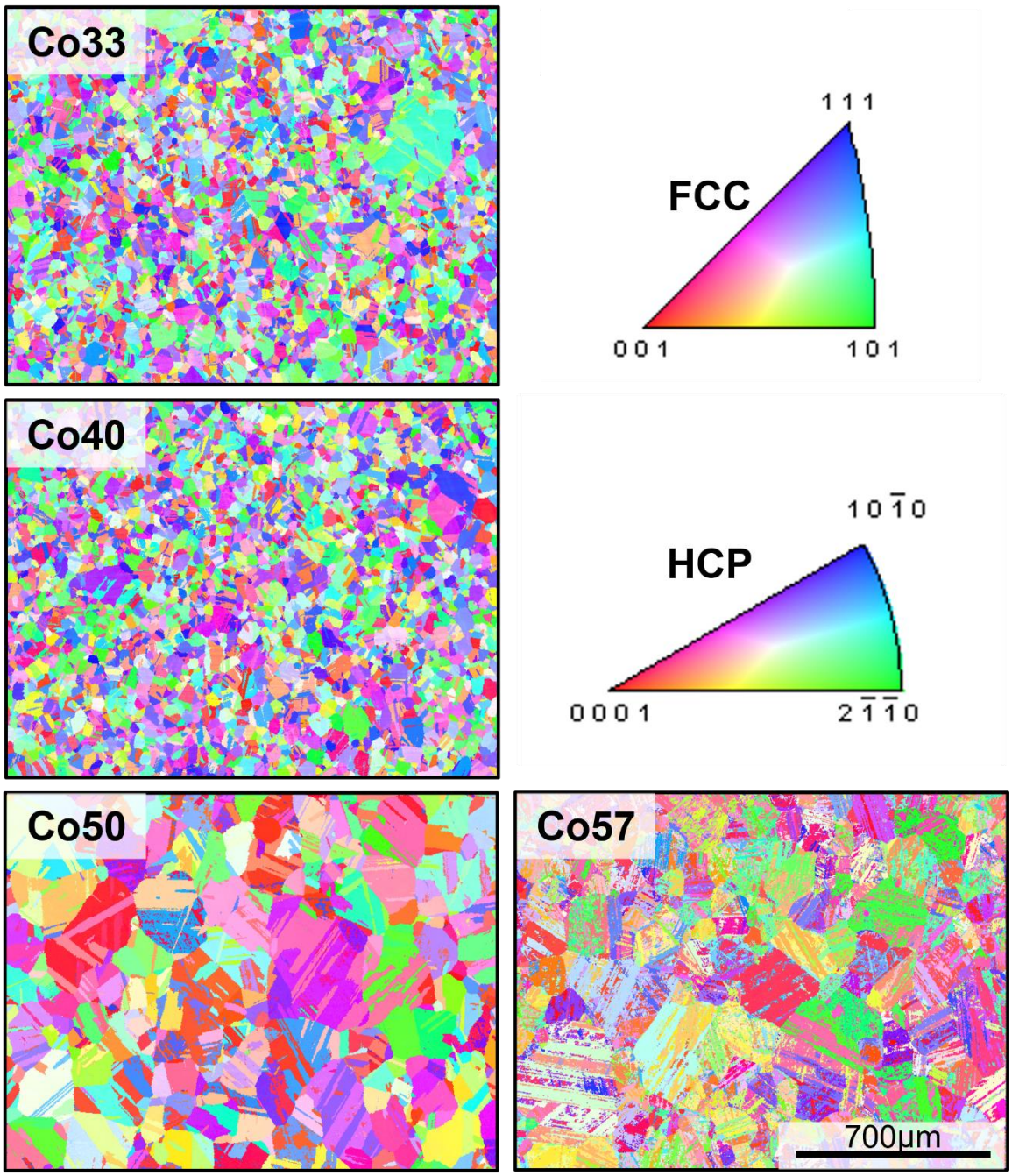

Figure III-2: EBSD IPF maps of the alloys in the pseudo-binary $Cr_{33}Co_xNi_{67-x}$ system in the as-annealed state.

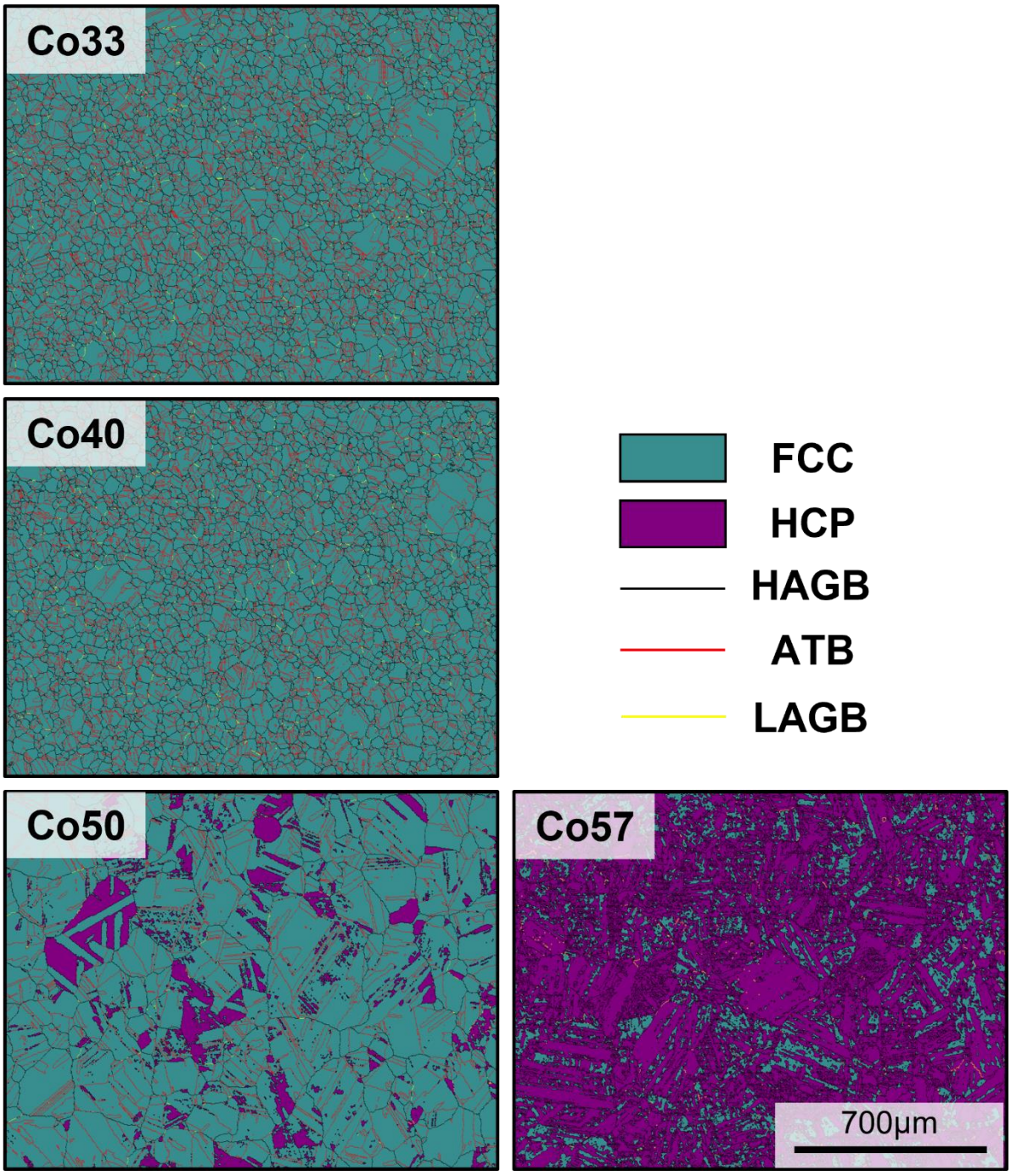

Figure III-3: EBSD phase maps of the alloys in the pseudo-binary $Cr_{33}Co_xNi_{67-x}$ system in the as-annealed state. The blue regions are FCC, and the purple are HCP. High-angle (>15°) grain and phase boundaries are marked with black lines, annealing twin boundaries with red and low-angle grain boundaries with yellow.

Table III-1: Grain size and crystallite size measured by linear intercept method using OIM EBSD analysis software. Grain size is a measure of the size of the FCC parent grains while crystallite size includes all annealing twin boundaries. Phase boundaries were not included for Co50 as they were polishing artifacts. Neither the grain size nor the crystallite size could be measured for Co57. Co50 and Co57 appear to have similar FCC parent grain sizes and the grain size of Co57 is estimated to be ~250μm.

	Grain Size (μm)	**Crystallite Size (μm)**
Co33	49	22
Co40	48	23
Co50	257	61
Co57	~250	-

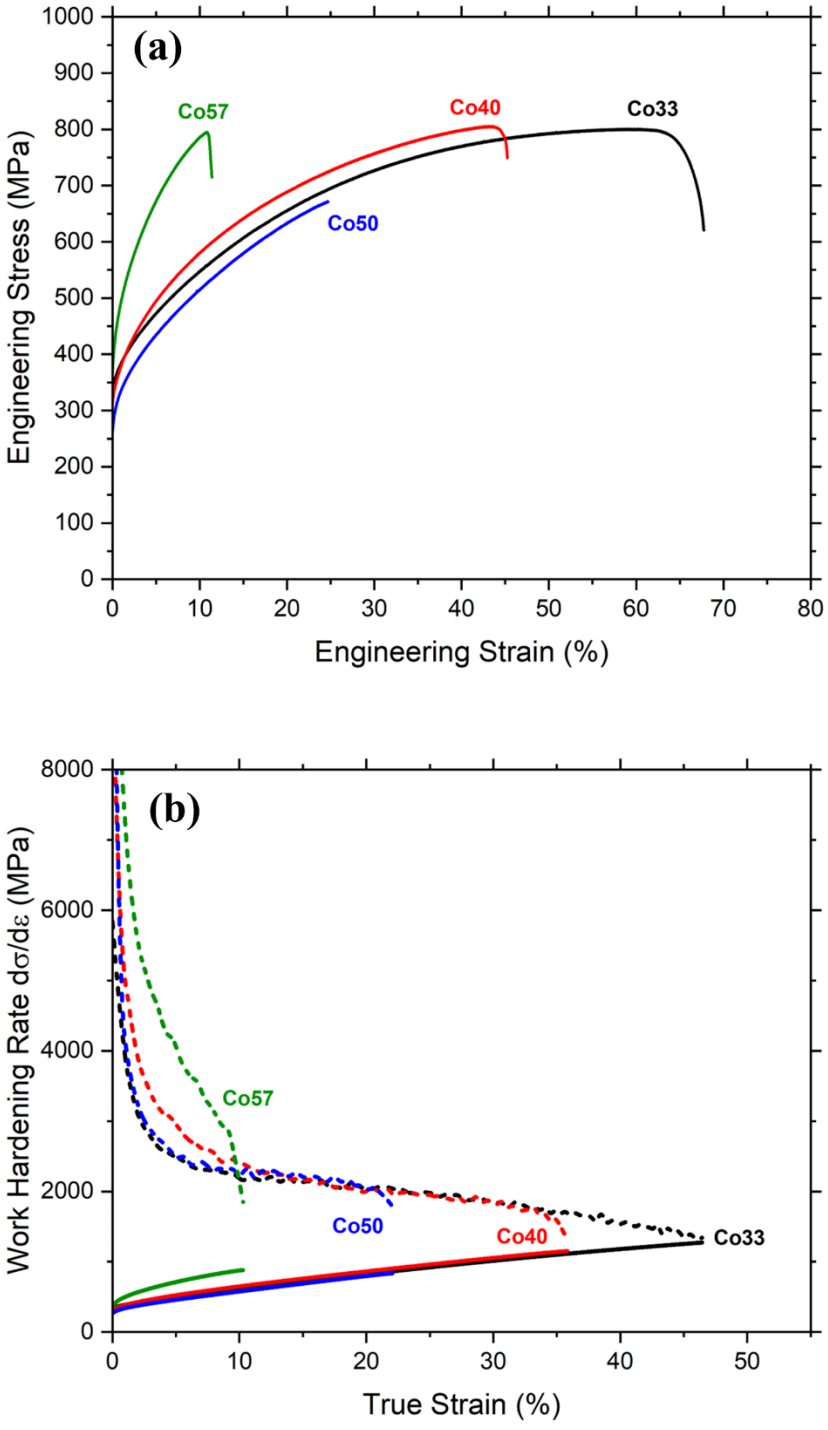

Figure III-4: (a) Representative engineering stress-strain curves. (b) Work hardening rates as a function of true stress (dashed) and the true stress-strain curves (solid). The work hardening rate and true stress-strain curves are calculated from the engineering curves (a).

Table III-2: Average tensile properties obtained from 3 tensile tests. Uncertainties are ±1 standard deviation. YS is yield strength; UTS is ultimate tensile strength; UE is uniform elongation; and EF is elongation to fracture.

	YS (MPa)	UTS (MPa)	UE (%)	EF (%)	True UTS (MPa)	True UE (%)
Co33	339 ± 8	801 ± 2	59 ± 3	70 ± 9	1273 ± 32	46 ± 2
Co40	314 ± 8	807 ± 12	47 ± 7	49 ± 7	1198 ± 75	39 ± 5
Co50	262 ± 8	678 ± 20	25 ± 1	25 ± 1	845 ± 30	22 ± 1
Co57	348 ± 24	776 ± 27	10 ± 1	11 ± 1	857 ± 35	9.9 ± 0.5

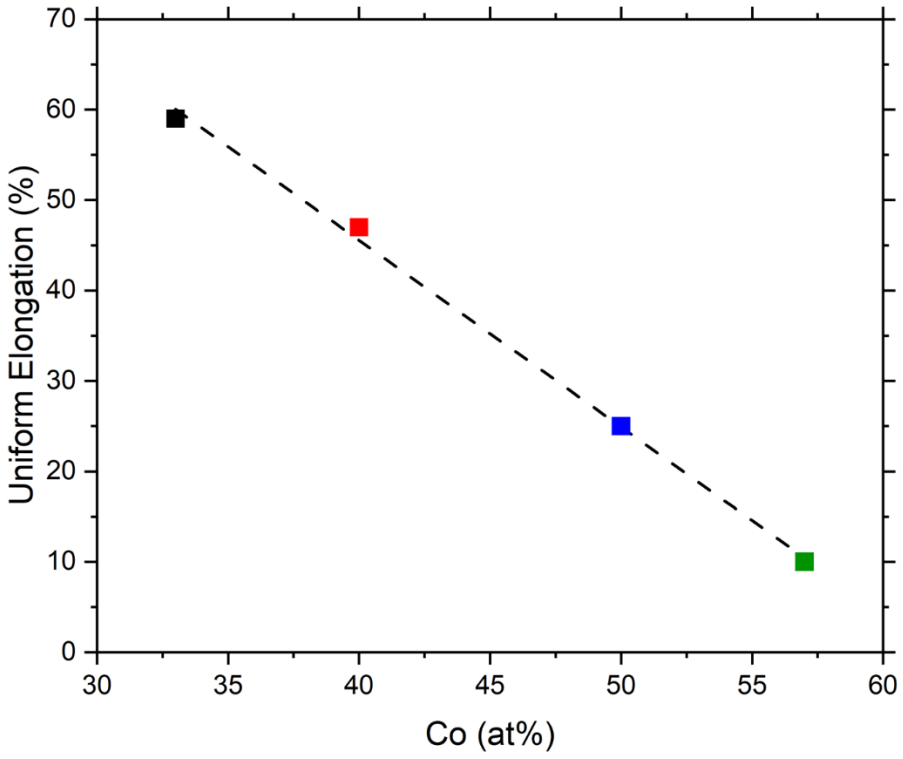

Figure III-5: Uniform elongation as a function of Co content. The color of each point corresponds to the color scheme used in the tensile data in Figure III-4. The dashed line is a best fit line with adjusted $R^2 = 0.997$.

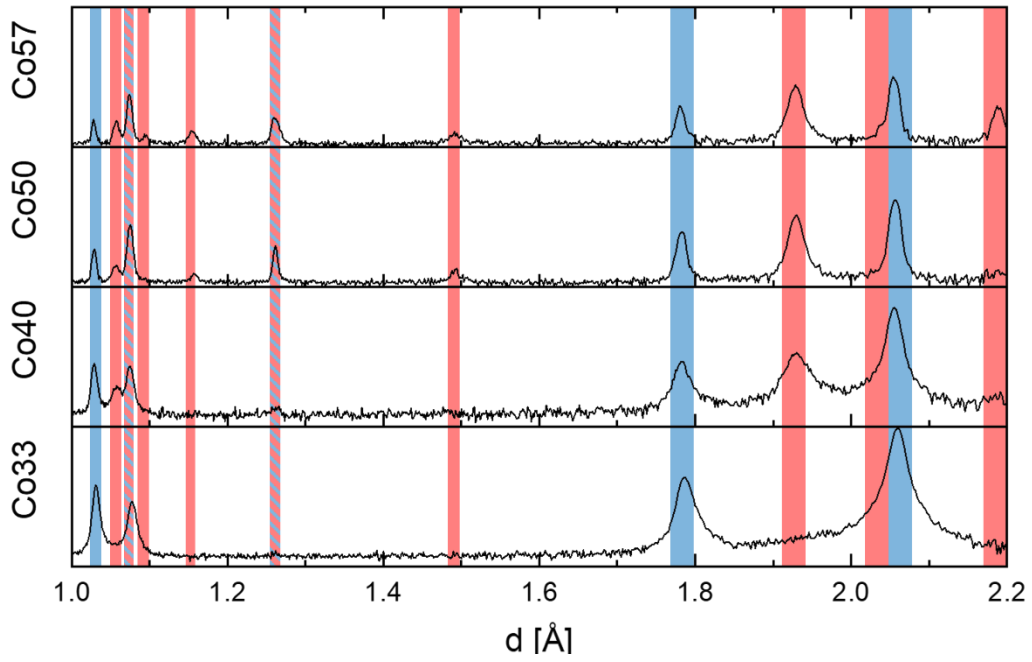

Figure III-6: Neutron diffraction patterns collected from the gauge section of fractured tensile specimens. The red bars indicate HCP reflections, and blue bars indicate FCC. The striped bars indicate shared FCC/HCP reflections.

Table III-3: The volume percent of HCP measured by neutron diffraction and Rietveld refinement. The thermally induced martensite was measured in the grip section of tensile specimens (that did not experience deformation during the tensile tests), and the total martensite was measured from the gauge sections of fracture tensile specimens. The deformation-induced HCP is the difference between the total HCP and thermally induced HCP.

	Thermally Induced HCP (vol%)	**Deformation Induced HCP (vol%)**	**Total HCP (vol%)**
Co33	0	0	0
Co40	0	29	29
Co50	0	49	49
Co57	23	39	62

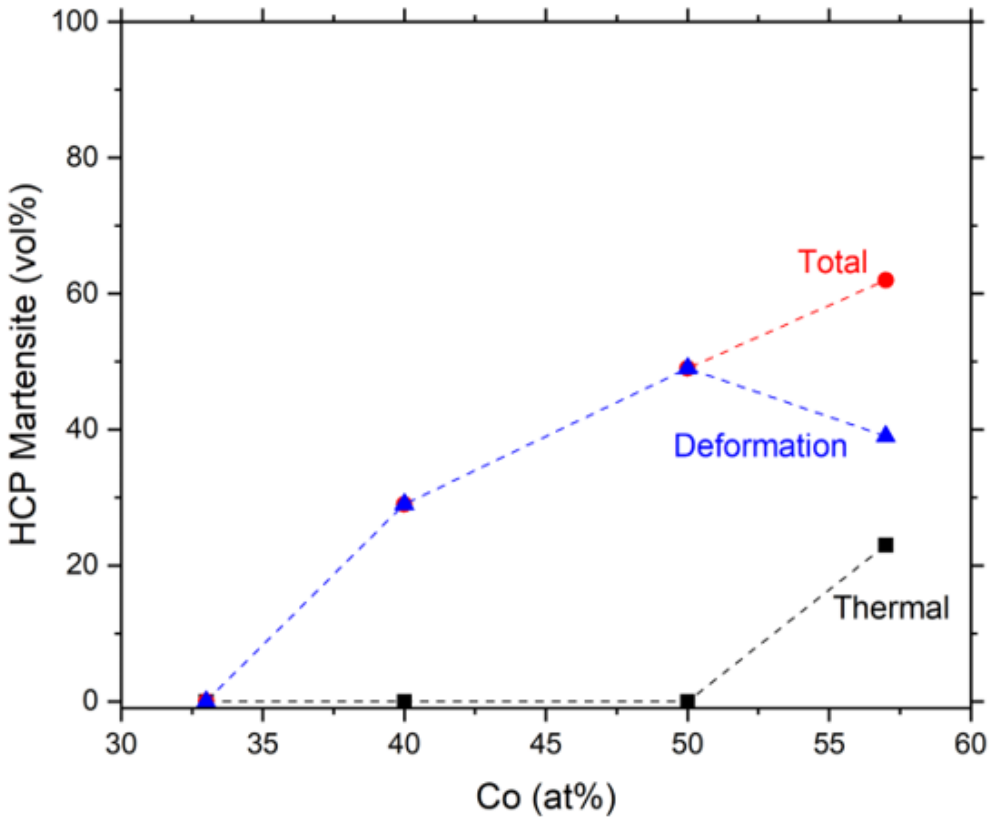

Figure III-7: The martensite content measured by neutron diffraction as a function of Co content. The dashed lines are not fitted and are intended to aid the eye.

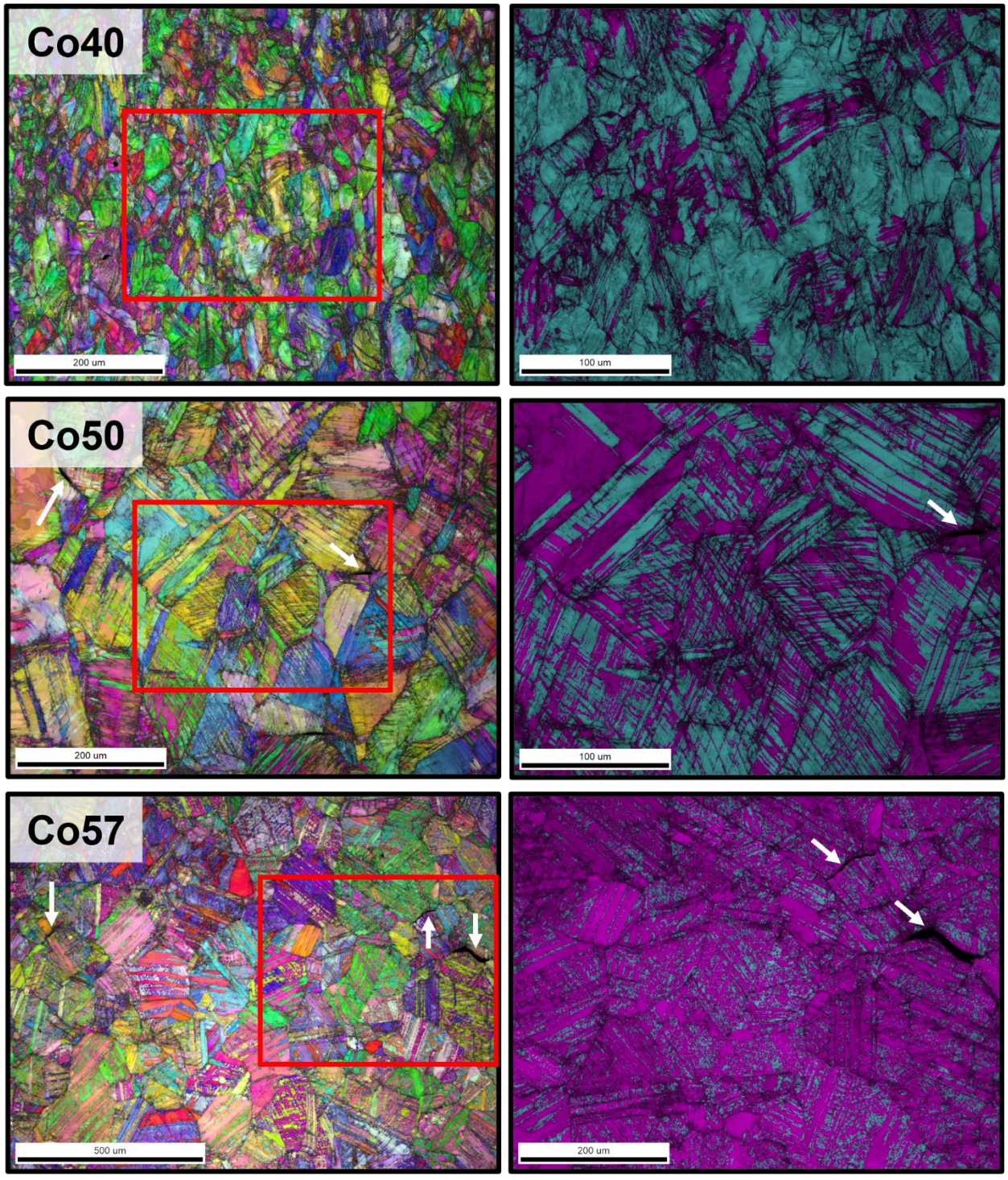

Figure III-8: (Left column) Post fracture IPF maps (left column) taken from the uniform portion of the gauge section. (Right column) Phase maps of the highlighted regions of the IPF maps. Blue regions are untransformed FCC and purple regions are HCP martensite. The white arrows highlight cracks formed at grain boundaries during tensile testing.

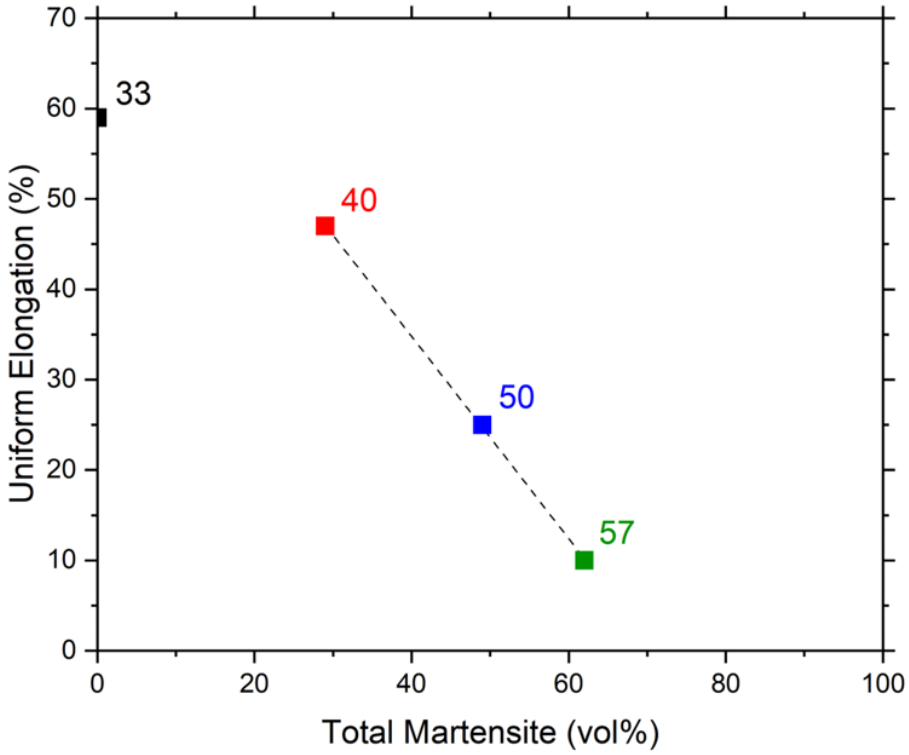

Figure III-9: Uniform elongation as a function of the volume percent of total HCP martensite measured after tensile testing. The dashed line is a best fit line through the Co40, Co50, and Co57 samples with an $R^2 = 1.000$. Co33 was excluded from the fit as it does not form any martensite.

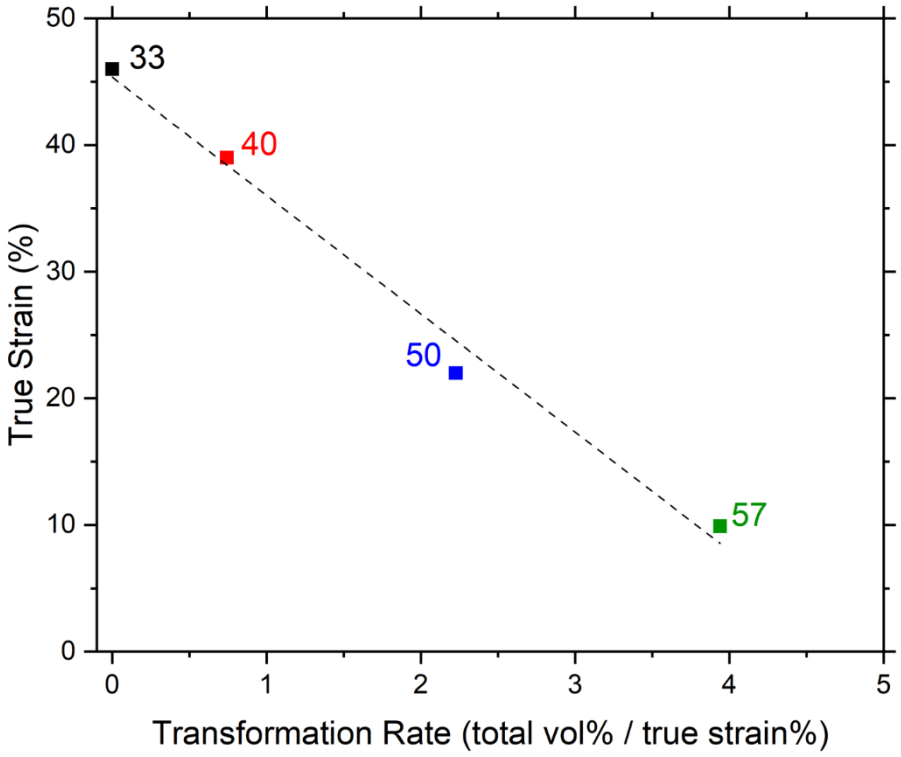

Figure III-10: True strain as a function of the average transformation rate (see text for context.) The dashed line is a best fit line with $R^2 = 0.983$.

Conclusion

This dissertation utilized two pseudo-binary HEA systems to investigate compositional effects on solid solution strengthening, TWIP, and TRIP, in a controlled manner. The unique challenges of modeling and understanding concentrated solid solutions were identified in Chapter I. Atomic displacements from ideal lattice sites offer a physically intuitive scaling factor for solid solution strengthening. Deformation-induced twinning and the TWIP effect were characterized in previously unexplored concentrated Cr-Co-Ni alloys, and their microstructure and mechanical properties were investigated in Chapter II. Co-rich Cr-Co-Ni alloys that undergo the FCC to HCP transformation were explored in Chapter III. It was found that this transformation severely reduces tensile elongation and does not promote the TRIP effect. HEAs offer immense alloy design freedom. The large compositional space with many elements presents more ‘knobs’ to turn in experimental design. This has opened the doors for new investigations and new insights in physical metallurgy.

References

[1] Z. Nishiyama, Martensitic Transformation, Academic Press, Inc (1978).
[2] Y. Tanaka, F. Pahlevani, S.C. Moon, R. Dippenaar, V. Sahajwalla, In situ characterisation of MnS precipitation in high carbon steel, Sci Rep 9 (2019) 12.
[3] B. Cantor, I.T.H. Chang, P. Knight, A.J.B. Vincent, Microstructural development in equiatomic multicomponent alloys, Mater. Sci. Eng. A-Struct. Mater. Prop. Microstruct. Process. 375 (2004) 213-218.
[4] J.W. Yeh, S.K. Chen, S.J. Lin, J.Y. Gan, T.S. Chin, T.T. Shun, C.H. Tsau, S.Y. Chang, Nanostructured high-entropy alloys with multiple principal elements: Novel alloy design concepts and outcomes, Adv. Eng. Mater. 6(5) (2004) 299-303.
[5] W. Hume-Rothery, G.W. Mabbott, K.M.C. Evans, The freezing points, melting points, and solid solubility limits of the alloys of silver and copper with the elements of the B sub-groups, Philos. Trans. R. Soc. Lond. A-Contain. Pap. Math. Phys. Character 233 (1934) 1-97.
[6] M.C. Troparevsky, J.R. Morris, M. Daene, Y. Wang, A.R. Lupini, G.M. Stocks, Beyond Atomic Sizes and Hume-Rothery Rules: Understanding and Predicting High-Entropy Alloys, Jom 67(10) (2015) 2350-2363.
[7] F. Otto, Y. Yang, H. Bei, E.P. George, Relative effects of enthalpy and entropy on the phase stability of equiatomic high-entropy alloys, Acta Mater. 61(7) (2013) 2628-2638.
[8] Z. Wu, H. Bei, G.M. Pharr, E.P. George, Temperature dependence of the mechanical properties of equiatomic solid solution alloys with face-centered cubic crystal structures, Acta Mater. 81 (2014) 428-441.
[9] Z.M. Li, K.G. Pradeep, Y. Deng, D. Raabe, C.C. Tasan, Metastable high-entropy dual-phase alloys overcome the strength-ductility trade-off, Nature 534(7606) (2016) 227-+.
[10] L. Remy, A. Pineau, TWINNING AND STRAIN-INDUCED FCC- HCP TRANSFORMATION IN FE-MN-CR-C SYSTEM, Materials Science and Engineering 28(1) (1977) 99-107.
[11] D.T. Pierce, J.T. Benzing, J.A. Jimenez, T. Hickel, I. Bleskov, J. Keum, D. Raabe, J.E. Wittig, The influence of temperature on the strain-hardening behavior of Fe-22/25/28Mn-3Al-3Si TRIP/TWIP steels, Materialia 22 (2022) 13.
[12] O. Grassel, L. Kruger, G. Frommeyer, L.W. Meyer, High strength Fe-Mn-(Al, Si) TRIP/TWIP steels development - properties - application, Int. J. Plast. 16(10-11) (2000) 1391-1409.
[13] C. Wagner, A. Ferrari, J. Schreuer, J.P. Couzinie, Y. Ikeda, F. Kormann, G. Eggeler, E.P. George, G. Laplanche, Effects of Cr/Ni ratio on physical properties of Cr-Mn-Fe-Co-Ni high-entropy alloys, Acta Mater. 227 (2022) 16.
[14] H.U. Jeong, N. Park, TWIP and TRIP-associated mechanical behaviors of Fe-x(CoCrMnNi)(100-x) medium-entropy ferrous alloys, Mater. Sci. Eng. A-Struct. Mater. Prop. Microstruct. Process. 782 (2020) 9.
[15] W. Fang, R.B. Chang, P.G. Ji, X. Zhang, B.X. Liu, X.H. Qu, F.X. Yin, Transformation Induced Plasticity Effects of a Non-Equal Molar Co-Cr-Fe-Ni High Entropy Alloy System, Metals 8(5) (2018) 10.
[16] J.W. Bae, J.M. Park, J. Moon, W.M. Choi, B.J. Lee, H.S. Kim, Effect of mu-precipitates on the microstructure and mechanical properties of non-equiatomic CoCrFeNiMo medium-entropy alloys, J. Alloy. Compd. 781 (2019) 75-83.

[17] J.W. Bae, J.B. Seol, J. Moon, S.S. Sohn, M.J. Jang, H.Y. Um, B.J. Lee, H.S. Kim, Exceptional phase-transformation strengthening of ferrous medium entropy alloys at cryogenic temperatures, Acta Mater. 161 (2018) 388-399.
[18] Y.H. Jo, W.M. Choi, D.G. Kim, A. Zargaran, S.S. Sohn, H.S. Kim, B.J. Lee, N.J. Kim, S. Lee, FCC to BCC transformation-induced plasticity based on thermodynamic phase stability in novel V10Cr10Fe45CoxNi35-x medium-entropy alloys, Sci Rep 9 (2019) 14.
[19] J. Yang, Y.H. Jo, D.W. Kim, W.M. Choi, H.S. Kim, B.J. Lee, S.S. Sohn, S. Lee, Effects of transformation-induced plasticity (TRIP) on tensile property improvement of Fe45Co30Cr10V10Ni5-xMnx high-entropy alloys, Mater. Sci. Eng. A-Struct. Mater. Prop. Microstruct. Process. 772 (2020) 9.
[20] D.X. Wei, X.Q. Li, S. Schonecker, J. Jiang, W.M. Choi, B.J. Lee, H.S. Kim, A. Chiba, H. Kato, Development of strong and ductile metastable face-centered cubic single-phase high-entropy alloys, Acta Mater. 181 (2019) 318-330.
[21] A. Durand, L. Peng, G. Laplanche, J.R. Morris, E.P. George, G. Eggeler, Interdiffusion in Cr-Fe-Co-Ni medium-entropy alloys, Intermetallics 122 (2020) 15.
[22] Dieter, Mechanical Metallurgy, (1986).
[23] N.F. Mott, F.R.N. Nabarro, An attempt to estimate the degree of precipitation hardening, with a simple model, Proc. Phys. Soc 52 (1940) 86-89.
[24] R.L. Fleischer, SOLUTION HARDENING, Acta Metallurgica 9(11) (1961) 996-1000.
[25] R. Labusch, STATISTICAL THEORIES OF SOLID-SOLUTION HARDENING, Acta Metallurgica 20(7) (1972) 917-&.
[26] R. Labusch, A STATISTICAL THEORY OF SOLID SOLUTION HARDENING, Physica Status Solidi 41(2) (1970) 659-&.
[27] G.P.M. Leyson, W.A. Curtin, L.G. Hector, C.F. Woodward, Quantitative prediction of solute strengthening in aluminium alloys, Nat. Mater. 9(9) (2010) 750-755.
[28] G.P.M. Leyson, L.G. Hector, W.A. Curtin, Solute strengthening from first principles and application to aluminum alloys, Acta Mater. 60(9) (2012) 3873-3884.
[29] G.P.M. Leyson, L.G. Hector, W.A. Curtin, First-principles prediction of yield stress for basal slip in Mg-Al alloys, Acta Mater. 60(13-14) (2012) 5197-5203.
[30] I. Toda-Caraballo, P.E.J. Rivera-Diaz-del-Castillo, Modelling solid solution hardening in high entropy alloys, Acta Mater. 85 (2015) 14-23.
[31] C. Varvenne, G.P.M. Leyson, M. Ghazisaeidi, W.A. Curtin, Solute strengthening in random alloys, Acta Mater. 124 (2017) 660-683.
[32] C. Varvenne, A. Luque, W.A. Curtin, Theory of strengthening in fcc high entropy alloys, Acta Mater. 118 (2016) 164-176.
[33] N.L. Okamoto, K. Yuge, K. Tanaka, H. Inui, E.P. George, Atomic displacement in the CrMnFeCoNi high-entropy alloy - A scaling factor to predict solid solution strengthening, AIP Adv. 6(12) (2016) 8.
[34] F.G. Coury, K.D. Clarke, C.S. Kiminami, M.J. Kaufman, A.J. Clarke, High Throughput Discovery and Design of Strong Multicomponent Metallic Solid Solutions, Sci Rep 8 (2018) 10.
[35] J.B. Nelson, D.P. Riley, AN EXPERIMENTAL INVESTIGATION OF EXTRAPOLATION METHODS IN THE DERIVATION OF ACCURATE UNIT-CELL DIMENSIONS OF CRYSTALS, Proceedings of the Physical Society of London 57(321) (1945) 160-177.
[36] B.D.S. Cullity, S. R., Elemenets of X-Ray Diffraction, Pearson Third Edition (2018).
[37] H.W. King, Quantitative Size-Factors for Metallic Solid Solutions, J. Mater. Sci. 1(1) (1966) 79-90.

[38] E.O. Hall, THE DEFORMATION AND AGEING OF MILD STEEL .3. DISCUSSION OF RESULTS, Proceedings of the Physical Society of London Section B 64(381) (1951) 747-753.
[39] N.J. Petch, THE CLEAVAGE STRENGTH OF POLYCRYSTALS, Journal of the Iron and Steel Institute 174(1) (1953) 25-28.
[40] N. Hansen, Hall-Petch relation and boundary strengthening, Scr. Mater. 51(8) (2004) 801-806.
[41] S. Yoshida, T. Ikeuchi, T. Bhattacharjee, Y. Bai, A. Shibata, N. Tsuji, Effect of elemental combination on friction stress and Hall-Petch relationship in face-centered cubic high / medium entropy alloys, Acta Mater. 171 (2019) 201-215.
[42] M. Schneider, E.P. George, T.J. Manescau, T. Zalezak, J. Hunfeld, A. Dlouhy, G. Eggeler, G. Laplanche, Analysis of strengthening due to grain boundaries and annealing twin boundaries in the CrCoNi medium-entropy alloy, Int. J. Plast. 124 (2020) 155-169.
[43] L. Remy, KINETICS OF FCC DEFORMATION TWINNING AND ITS RELATIONSHIP TO STRESS-STRAIN BEHAVIOR, Acta Metallurgica 26(3) (1978) 443-451.
[44] O. Bouaziz, N. Guelton, Modelling of TWIP effect on work-hardening, Mater. Sci. Eng. A-Struct. Mater. Prop. Microstruct. Process. 319 (2001) 246-249.
[45] L. Remy, A. Pineau, TWINNING AND STRAIN-INDUCED FCC- HCP TRANSFORMATION ON MECHANICAL-PROPERTIES OF CO-NI-CR-MO ALLOYS, Materials Science and Engineering 26(1) (1976) 123-132.
[46] O. Grassel, G. Frommeyer, Effect of martensitic phase transformation and deformation twinning on mechanical properties of Fe-Mn-Si-Al steels, Mater. Sci. Technol. 14(12) (1998) 1213-1217.
[47] I. Gutierrez-Urrutia, D. Raabe, Dislocation and twin substructure evolution during strain hardening of an Fe-22 wt.% Mn-0.6 wt.% C TWIP steel observed by electron channeling contrast imaging, Acta Mater. 59(16) (2011) 6449-6462.
[48] D.T. Pierce, J.A. Jimenez, J. Bentley, D. Raabe, J.E. Wittig, The influence of stacking fault energy on the microstructural and strainhardening evolution of Fe-Mn-Al-Si steels during tensile deformation, Acta Mater. 100 (2015) 178-190.
[49] B.C. De Cooman, Y. Estrin, S.K. Kim, Twinning-induced plasticity (TWIP) steels, Acta Mater. 142 (2018) 283-362.
[50] T.S. Byun, On the stress dependence of partial dislocation separation and deformation microstructure in austenitic stainless steels, Acta Mater. 51(11) (2003) 3063-3071.
[51] S. Allain, J.P. Chateau, O. Bouaziz, S. Migot, N. Guelton, Correlations between the calculated stacking fault energy and the plasticity mechanisms in Fe-Mn-C alloys, Mater. Sci. Eng. A-Struct. Mater. Prop. Microstruct. Process. 387 (2004) 158-162.
[52] M. Pozuelo, J.E. Wittig, J.A. Jimenez, G. Frommeyer, Enhanced Mechanical Properties of a Novel High-Nitrogen Cr-Mn-Ni-Si Austenitic Stainless Steel via TWIP/TRIP Effects, Metall. Mater. Trans. A-Phys. Metall. Mater. Sci. 40A(8) (2009) 1826-1834.
[53] A.S. Hamada, L.P. Karjalainen, R.D.K. Misra, J. Talonen, Contribution of deformation mechanisms to strength and ductility in two Cr-Mn grade austenitic stainless steels, Mater. Sci. Eng. A-Struct. Mater. Prop. Microstruct. Process. 559 (2013) 336-344.
[54] W.N. Roberts, DEFORMATION TWINNING IN HADFIELD STEEL, Transactions of the Metallurgical Society of Aime 230(3) (1964) 372-&.
[55] P. Anderson, J. Hirth, J. Lothe, Theory of Dislocations, 3rd ed.2017.
[56] J.W. Christian, S. Mahajan, DEFORMATION TWINNING, Prog. Mater. Sci. 39(1-2) (1995) 1-157.

[57] J.A. Venables, DEFORMATION TWINNING IN FACE-CENTRED CUBIC METALS, Philosophical Magazine 6(63) (1961) 379-396.
[58] D.R. Steinmetz, T. Japel, B. Wietbrock, P. Eisenlohr, I. Gutierrez-Urrutia, A. Saeed-Akbari, T. Hickel, F. Roters, D. Raabe, Revealing the strain-hardening behavior of twinning-induced plasticity steels: Theory, simulations, experiments, Acta Mater. 61(2) (2013) 494-510.
[59] G. Laplanche, A. Kostka, O.M. Horst, G. Eggeler, E.P. George, Microstructure evolution and critical stress for twinning in the CrMnFeCoNi high-entropy alloy, Acta Mater. 118 (2016) 152-163.
[60] G. Laplanche, A. Kostka, C. Reinhart, J. Hunfeld, G. Eggeler, E.P. George, Reasons for the superior mechanical properties of medium-entropy CrCoNi compared to high-entropy CrMnFeCoNi, Acta Mater. 128 (2017) 292-303.
[61] J.W. Brooks, M.H. Loretto, R.E. Smallman, DIRECT OBSERVATIONS OF MARTENSITE NUCLEI IN STAINLESS-STEEL, Acta Metallurgica 27(12) (1979) 1839-1847.
[62] L. Remy, A. Pineau, TEMPERATURE-DEPENDENCE OF STACKING-FAULT ENERGY IN CLOSE-PACKED METALS AND ALLOYS, Materials Science and Engineering 36(1) (1978) 47-63.
[63] E.H. Koster, A. Howie, A.R. Tholen, STACKING FAULT ENERGIES OF NI-CO-CR ALLOYS, Philosophical Magazine 10(108) (1964) 1093-&.
[64] F. Otto, A. Dlouhy, C. Somsen, H. Bei, G. Eggeler, E.P. George, The influences of temperature and microstructure on the tensile properties of a CoCrFeMnNi high-entropy alloy, Acta Mater. 61(15) (2013) 5743-5755.
[65] F. Otto, N.L. Hanold, E.P. George, Microstructural evolution after thermomechanical processing in an equiatomic, single-phase CoCrFeMnNi high-entropy alloy with special focus on twin boundaries, Intermetallics 54 (2014) 39-48.
[66] B. Gludovatz, A. Hohenwarter, K.V.S. Thurston, H.B. Bei, Z.G. Wu, E.P. George, R.O. Ritchie, Exceptional damage-tolerance of a medium-entropy alloy CrCoNi at cryogenic temperatures, Nat. Commun. 7 (2016) 8.
[67] G. Bertoli, L.B. Otani, A.J. Clarke, C.S. Kiminami, F.G. Coury, Hall-Petch and grain growth kinetics of the low stacking fault energy TRIP Cr40Co40Ni20 multi-principal element alloy, Appl. Phys. Lett. 119(6) (2021) 7.
[68] Y.P. Varshni, Temperature dependence of the elastic constants, Physical Review B-Solid State 2(10) (1970) 3952-3958.
[69] G. Laplanche, P. Gadaud, C. Barsch, K. Demtroder, C. Reinhart, J. Schreuer, E.P. George, Elastic moduli and thermal expansion coefficients of medium-entropy subsystems of the CrMnFeCoNi high-entropy alloy, J. Alloy. Compd. 746 (2018) 244-255.
[70] K. Sipos, L. Remy, A. Pineau, INFLUENCE OF AUSTENITE PREDEFORMATION ON MECHANICAL-PROPERTIES AND STRAIN-INDUCED MARTENSITIC TRANSFORMATIONS OF A HIGH MANGANESE STEEL, Metallurgical Transactions a-Physical Metallurgy and Materials Science 7(6) (1976) 857-864.
[71] G.B. Olson, W.S. Owen, Martensite, ASM International1992.
[72] S. Martin, S. Wolf, U. Martin, L. Kruger, D. Rafaja, Deformation Mechanisms in Austenitic TRIP/TWIP Steel as a Function of Temperature, Metall. Mater. Trans. A-Phys. Metall. Mater. Sci. 47A(1) (2016) 49-58.
[73] J.F. Breedis, L. Kaufman, FORMATION OF HCP AND BCC PHASES IN AUSTENITIC IRON ALLOYS, Metallurgical Transactions 2(9) (1971) 2359-+.

[74] H.F. Lopez, A.J. Saldivar-Garcia, Martensitic transformation in a cast Co-Cr-Mo-C alloy, Metall. Mater. Trans. A-Phys. Metall. Mater. Sci. 39A(1) (2008) 8-18.
[75] A. Mani, R. Salinas, H.F. Lopez, Deformation induced FCC to HCP transformation in a Co-27Cr-5Mo-0.05C alloy, Mater. Sci. Eng. A-Struct. Mater. Prop. Microstruct. Process. 528(7-8) (2011) 3037-3043.
[76] Y. Koizumi, S. Suzuki, K. Yamanaka, B.S. Lee, K. Sato, Y.P. Li, S. Kurosu, H. Matsumoto, A. Chiba, Strain-induced martensitic transformation near twin boundaries in a biomedical Co-Cr-Mo alloy with negative stacking fault energy, Acta Mater. 61(5) (2013) 1648-1661.
[77] K. Yoda, Suyalatu, A. Takaichi, N. Nomura, Y. Tsutsumi, H. Doi, S. Kurosu, A. Chiba, Y. Igarashi, T. Hanawa, Effects of chromium and nitrogen content on the microstructures and mechanical properties of as-cast Co-Cr-Mo alloys for dental applications, Acta Biomater. 8(7) (2012) 2856-2862.
[78] R.G. Stringfellow, D.M. Parks, G.B. Olson, A CONSTITUTIVE MODEL FOR TRANSFORMATION PLASTICITY ACCOMPANYING STRAIN-INDUCED MARTENSITIC TRANSFORMATIONS IN METASTABLE AUSTENITIC STEELS, Acta Metall. Mater. 40(7) (1992) 1703-1716.
[79] L. Samek, E. De Moor, J. Penning, B.C. De Cooman, Influence of alloying elements on the kinetics of strain-induced martensitic nucleation in low-alloy, multiphase high-strength steels, Metall. Mater. Trans. A-Phys. Metall. Mater. Sci. 37A(1) (2006) 109-124.
[80] P.J. Gibbs, E. De Moor, M.J. Merwin, B. Clausen, J.G. Speer, D.K. Matlock, Austenite Stability Effects on Tensile Behavior of Manganese-Enriched-Austenite Transformation-Induced Plasticity Steel, Metall. Mater. Trans. A-Phys. Metall. Mater. Sci. 42A(12) (2011) 3691-3702.
[81] D.X. Wei, X.Q. Li, W.C. Heng, Y. Koizumi, F. He, W.M. Choi, B.J. Lee, H.S. Kim, H. Kato, A. Chiba, Novel Co-rich high entropy alloys with superior tensile properties, Mater. Res. Lett. 7(2) (2019) 82-88.
[82] F.G. Coury, D. Santana, Y.F. Guo, J. Copley, L. Otani, S. Fonseca, G. Zepon, C. Kiminami, M. Kaufman, A. Clark, Design and in-situ characterization of a strong and ductile co-rich multicomponent alloy with transformation induced plasticity, Scr. Mater. 173 (2019) 70-74.
[83] H.W. Deng, M.M. Wang, Z.M. Xie, T. Zhang, X.P. Wang, Q.F. Fang, Y. Xiong, Enhancement of strength and ductility in non-equiatomic CoCrNi medium-entropy alloy at room temperature via transformation-induced plasticity, Mater. Sci. Eng. A-Struct. Mater. Prop. Microstruct. Process. 804 (2021) 11.
[84] J.A. Copley, F.G. Coury, B. Ellyson, J. Klemm-Toole, J. Frishkoff, C. Finfrock, Z. Fisher, N. Kedir, C. Kirk, W. Chen, N. Parab, T. Sun, K. Fezzaa, K.D. Clarke, A.J. Clarke, In-Situ Observation of FCC -> HCP Transformation-Induced Plasticity Behavior During Dynamic Deformation of CoCrNi Multi-principal Element Alloys, Metall. Mater. Trans. A-Phys. Metall. Mater. Sci. 53(5) (2022) 1821-1830.
[85] Z.J. Gu, Y.Z. Tian, W. Xu, S. Lu, X.L. Shang, J.W. Wang, G.W. Qin, Optimizing transformation-induced plasticity in CoCrNi alloys by combined grain refinement and chemical tuning, Scr. Mater. 214 (2022) 5.
[86] Y. Yang, T.Y. Chen, L.Z. Tan, J.D. Poplawsky, K. An, Y.L. Wang, G.D. Samolyuk, K. Littrell, A.R. Lupini, A. Borisevich, E.P. George, Bifunctional nanoprecipitates strengthen and ductilize a medium-entropy alloy, Nature 595(7866) (2021) 245-+.
[87] W. Zhong, Y. Yang, S. Hayakawa, H. Xu, K. An, I. Stinson, A.Y. Borisevich, J.L. Cicotte, E.P. George, A novel alloy design strategy involving multistep phase transformations and nanotwinning for enhanced mechanical properties, Oak Ridge National Laboratory, 2022.

[88] K. An, VDRIVE - Data Reduction and Interactive Visualization Software for Event Mode Neutron Diffraction, ORNL Report, Oak Ridge National Laboratory, ORNL-TM-2012-621, 2012.
[89] L. A.C., R.B. Von Dreele, General Structure Analysis System (GSAS), Los Alamos National Laboratory Report, 2000.
[90] B.H. Toby, EXPGUI, a graphical user interface for GSAS, J. Appl. Cryst., 2001, pp. 210-213.
[91] B.L. Yin, S. Yoshida, N. Tsuji, W.A. Curtin, Yield strength and misfit volumes of NiCoCr and implications for short-range-order, Nat. Commun. 11(1) (2020) 7.
[92] H.Y. He, M. Naeem, F. Zhang, Y.L. Zhao, S. Harjo, T. Kawasaki, B. Wang, X.L. Wu, S. Lan, Z.D. Wu, W. Yin, Y. Wu, Z.P. Lu, J.J. Kai, C.T. Liu, X.L. Wang, Stacking Fault Driven Phase Transformation in CrCoNi Medium Entropy Alloy, Nano Lett. 21(3) (2021) 1419-1426.
[93] C.N. Niu, C.R. LaRosa, J.S. Miao, M.J. Mills, M. Ghazisaeidi, Magnetically-driven phase transformation strengthening in high entropy alloys, Nat. Commun. 9 (2018) 9.
[94] M. Koyama, T. Sawaguchi, K. Tsuzaki, Premature Fracture Mechanism in an Fe-Mn-C Austenitic Steel, Metall. Mater. Trans. A-Phys. Metall. Mater. Sci. 43A(11) (2012) 4063-4074.
[95] M. Koyama, T. Sawaguchi, K. Tsuzaki, TWIP Effect and Plastic Instability Condition in an Fe-Mn-C Austenitic Steel, ISIJ Int. 53(2) (2013) 323-329.
[96] B.S. Lee, H. Matsumoto, A. Chiba, Fractures in tensile deformation of biomedical Co-Cr-Mo-N alloys, Mater. Lett. 65(5) (2011) 843-846.
[97] S. Kurosu, H. Matsumoto, A. Chiba, C. Landron, D. Fabregue, E. Maire, The damage process in a biomedical Co-29Cr-6Mo-0.14N alloy analyzed by X-ray tomography and electron backscattered diffraction, Scr. Mater. 64(5) (2011) 367-370.
[98] S. Basu, Z.M. Li, K.G. Pradeep, D. Raabe, Strain Rate Sensitivity of a TRIP-Assisted Dual-Phase High-Entropy Alloy, Front. Mater. 5 (2018) 10.
[99] Z.M. Li, C.C. Tasan, K.G. Pradeep, D. Raabe, A TRIP-assisted dual-phase high-entropy alloy: Grain size and phase fraction effects on deformation behavior, Acta Mater. 131 (2017) 323-335.

Vita

Joshua Lee Cicotte was born in Michigan to the parents of Jeff and Kristen Cicotte. He graduated from Allen Park High School in 2013. He received his BS in Materials Science and Engineering from the Michigan Technological University in the spring of 2017. He briefly held an STA Site Engineering position at Ford Motor Company before continuing to graduate school at the University of Tennessee Knoxville in January 2018. Josh earned his MS in December of 2019 and his PhD in December of 2022, both in Materials Science and Engineering from the University of Tennessee. His dissertation focused on the mechanical properties of high entropy alloys, and he performed his research at the Oak Ridge National Laboratory in the Alloy Behavior and Design group.